Treatment of polar grid singularities in the bi-cubic Hermite-Bézier approximations: isoparametric finite element framework

Ashish Bhole, Boniface Nkonga, Stanislas Pamela, Guido Huijsmans, Matthias Hoelzl

Treatment of polar grid singularities in the bi-cubic Hermite-Bézier approximations: isoparametric finite element framework

Ashish Bhole[1], Boniface Nkonga[2], Stanislas Pamela[3], Guido Huijsmans[4,5], Matthias Hoelzl[6], and JOREK team[7]

[1,2]Université Côte d'Azur (UCA), JAD/C.N.R.S. U.M.R. 7351, Parc Valrose, 06108 NICE Cedex 2, France
[3]CCFE, Culham Science Centre, Abingdon, Oxon, OX14 3DB, UK
[4]CEA, IRFM, F-13108 Saint-Paul-lez-Durance, France
[5]Eindhoven University of Technology, PO Box 513, 5600 MB Eindhoven, Netherlands
[6]Max-Planck Institute for Plasma Physics, Garching, Germany
[7]See [1] for the present list of team members

Abstract

We propose a numerical treatment for the geometric singularity at the polar grid center encountered in the application of the isoparametric bi-cubic Hemite Bézier finite element method. The treatment applies a set of new basis functions at the polar grid center in the numerical algorithm where the new basis functions are simply the linear transformations of the original basis functions. The linear transformation comes out naturally by analyzing the interpolation formula at the polar grid center. The proposed polar treatment enforces the C^1 regularity in the physical space and preserves the order of the accuracy of the interpolation. The treatment is applied in the nonlinear MHD code JOREK. With the help of a range of numerical tests, it is demonstrated that the polar treatment improves the stability and accuracy of the numerical approximation near the polar grid center. The polar treatment presented can be applied to the grid center of circular or non-circular polar grids and is also applicable for the bi-cubic Hermite finite element method.

Keywords

Polar grid singularities, Isoparametric mapping, bi-cubic Hemite Bézier Finite element method, Magnetic flux surface aligned grid, Magneto-hydrodynamics, MHD instabilities in tokamaks

1 Introduction

When governing equations are expressed in the cylindrical or spherical coordinate systems, for efficiency, their numerical approximations may also be based on the symmetries in the coordinate systems. It is advantageous to formulate the numerical approximations on the grids that are aligned with the coordinate symmetries. Such an alignment is often achieved through a geometrical transformation that maps a parametric domain onto a physical space. For cylindrical or spherical coordinate system, a geometric transformation inevitably produces geometrical singularities, even when there is no reason for governing equations to be singular, and leads to difficulties in the development of consistent and accurate numerical approximations. Therefore particular attention must be paid to the numerical approximation in the vicinity of the geometrical singularities. A typical situation that encounters a geometric singularity is the polar grids. For the cylindrical symmetry, the geometric singularity is expressed in terms of the limit of the function $1/r$ when the radial distance (r) tends to zero. Numerical approximations in this limit may create numerical instabilities at the polar grid center that can pollute the numerical solution and adversely affect the stability of a numerical algorithm.

Depending upon the numerical methods and physical applications, many strategies to handle the numerical difficulties at the geometric center of the polar grids are available in the literature. In the context of finite difference methods, Griffin et al. [2] use the L'Hôpital rule on the terms with $1/r$, Mohseni and Colonius [3] use the geometric transformation to avoid the point at $r = 0$, Constantinescu and Lele [4] derive a new set of equations at the polar axis using series expansion, Prochnow et al. [5] use staggered grids to avoid the point of singularity and in [6] parity conditions for flow equations in the azimuthal Fourier modes are derived. In the context of pseudo-spectral approximations, Huang and Sloan [7] develop pole conditions based on the solution smoothness, while Serre and Pulicani [8] use a strategy based on the change of variables to remove the polar singularity. In the context of spectral methods, Mercader et al. [9] use parity of Fourier modes in the numerical scheme such that no additional treatment for the polar singularity is needed while the stable and accurate formulation is obtained at the same time. In the context of finite volume methods, Asaithambi and Mahesh [10] merge the cells on the polar grid center to improve the stability conditions. In the context of finite element methods, Olson et al. [11] present a few strategies to treat the singularities encountered in finite element applications in general. Most of the numerical treatments cited above are achieved in the framework of spectral methods and mainly applied to the simulations of incompressible turbulent flows [12]. Some of the treatments may not preserve the stability of the associated numerical methods and the clustering of the grid points in the radial direction at the grid center may be required to improve the accuracy of the method. Olson et al. in [11] state that *In both the finite difference and the finite element methods, local refinement is often employed near the singularity to achieve reasonable accuracy. However, the accuracy achieved and the rate of convergence are generally not uniform nor satisfactory.* In the isogeometric analysis (IGA) framework, techniques to construct polar splines basis functions that are C^k smooth everywhere, including geometrically singular polar points, have been developed [13, 14]. Smoothness constraints at singular polar points are enforced via an extraction operator $\bar{\boldsymbol{E}}^k$ that takes a linear combination of underlying basis functions at the polar center. The smooth polar spline framework developed in [13, 14] has been applied to solve the ideal magneto-hydrodynamics (MHD) eigenvalue problem for axisymmetric equilibria [15] that lead to a continuous description of eigenfunctions across the polar grid center.

We will now focus on the particular case of the singularity at the polar grid center encountered in the numerical simulation of the magneto-hydrodynamics (MHD) equations for the plasmas in tokamak modeling. In magnetic fusion devices such as tokamaks, the plasma is expected to be confined in that device to harness the fusion energy. Unfortunately, the large-scale plasma

instabilities disturb the plasma confinement and their control is a major challenge in fusion experiments. Understanding the plasma instabilities and developing effective control strategies is one of the urgent requirements on the path towards feasible fusion power plants [1]. Computational tools can play a key role in providing an insight into relevant plasma dynamics and help understand the nature of these instabilities. JOREK [16] is one of the nonlinear MHD codes that has been developed to simulate the plasma dynamics in magnetic fusion devices and uses polar grids. Owing to the torus-shaped geometry of a tokamak device, the MHD equations are written into the cylindrical (or toroidal) coordinate system. In a typical numerical simulation using JOREK, the MHD instabilities are investigated starting the self-consistent time evolution of the equations from an equilibrium state that is governed by the so-called Grad-Shafranov equation [17] (GSE). It is a nonlinear elliptic equation that determines the profiles for the poloidal magnetic flux surfaces (ψ). The plasma dynamics in tokamaks is strongly constrained by these flux surfaces and hence it is advantageous to develop numerical strategies that use grids aligned with these flux surfaces. The grid generators in the code JOREK can construct such flux-aligned grids in the poloidal plane, the plane orthogonal to the toroidal direction (ϕ) (see Figure (1a)). An option to extend the grids to the true physical walls is also available [18]. JOREK uses C^1-finite element approximation in the poloidal plane while Fourier representation in the periodic ϕ direction to solve mainly nonlinear MHD equations. The code has been extensively used for tokamak modeling and a wide range of its applications are presented in [1] and references therein. In the framework of isoparametric analysis, the finite element space in the poloidal plane is based on a bi-cubic Hermite-Bézier basis function which was originally proposed in [16] as a necessary developmental step for JOREK. The properties of this finite element space have been investigated in [19, 20]. Recently the extension to the higher-order Hermite-Bézier polynomials has been implemented successfully and was shown to reduce the computational costs to reach the same level of accuracy [21]. The main idea of the approach used in JOREK is to define the physical domain (poloidal plane) by a nonlinear transformation of a parametric domain which is decomposed into quadrangular elements. This transformation is constructed from the same finite element space as the one used for the interpolation of the different variables of the problem: isoparametric finite element formulation. The resulting grids in the physical space contain the curved quadrangular elements with C^1 regularity, except at some special points that include the singular polar grid center.

For realistic tokamak geometries, the plasma equilibrium configuration also motivates the construction of multi-block grids [22]. The plasma equilibrium state contains the critical points, extrema, or saddle points characterized by $\nabla\psi = 0$, which can be used to decompose the domain into concentric, non-overlapping, closed flux surfaces and open, non-overlapping open flux surfaces (for the details see [23]). A typical example of the plasma equilibrium state is shown in Figure (1b). A block with closed, concentric flux surfaces leads to a grid that is isomorphic to a polar grid and has a geometric singularity at its center. Unfortunately, a typical flux-aligned multi-block grid has at least one block with a polar grid. While a flux-aligned multi-block grid is a specific case used in JOREK, the use of general polar grids is also a possibility. Until now, for most of the numerical simulations, quite satisfactory numerical results have been obtained with a simple treatment of the polar grid singularity which enforces the continuity of the functions at the symmetry axis [1]. However, this crude treatment locally degrades the numerical properties of the finite element method (FEM) and may generate numerical instabilities for convection-dominated flows polluting the entire numerical solution. Unstructured grids that are not aligned with the flux surfaces avoid the geometrical singularities and offer greater flexibility in terms of modeling complex geometries, local refinement, etc. However numerical algorithms using such grids may lead to spurious numerical diffusion and hence higher order approximation is needed. An approach that avoids singularities and uses hybrid discontinuous Galerkin method based on

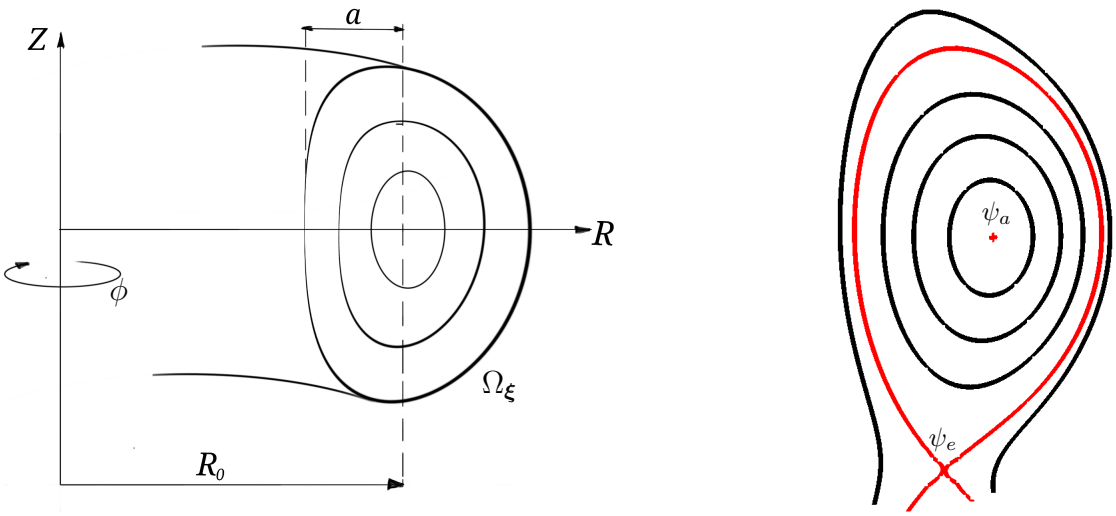

(a) (b)

Figure 1: a) Toroidal domain: $\Omega = \Omega_{\boldsymbol{\xi}} \times \Omega_\phi$ where $\Omega_{\boldsymbol{\xi}} = (R, Z)^{\mathrm{T}}$. b) An example of an ideal MHD equilibrium state on $\Omega_{\boldsymbol{\xi}}$ governed by GSE with iso-surfaces for the magnetic flux ψ shown. The point ψ_0 marked in red color denotes the location of the magnetic axis and the point ψ_e denotes the location of the saddle point in ψ field. Both points are characterized by $\nabla\psi = 0$. The contour in red color passing through ψ_e denotes the separatrix. Inside the separatrix, flux surfaces are closed, while the flux surfaces outside the separatrix intersect with the physical walls.

curved elements in the poloidal plane is presented in [24, 25].

In this work, we propose an efficient and accurate approach to overcome numerical difficulties related to the singularity at the polar grid center for the bicubic Hermite Bézier FEM. The proposed strategy can be viewed as a change of variables and leads to the enforcing of the C^1 regularity at the axis of symmetry in the physical space directly. The rest of the paper is organized as follows. We start by briefly recalling the bi-cubic Hermite-Bézier FEM developed in [16]. Then the singularity at the symmetry axis is investigated as an asymptotic limit of an annular mesh where the radius of the hole goes to zero. This analysis leads to the reformulation of the basis functions as a linear combination of the original basis functions. Then the associated new degrees of freedom are the variables and their gradients in the physical space. We show that the proposed strategy at the polar grid center preserves the accuracy of the original interpolation and is straightforward to apply. We note the similarities of the proposed polar treatment with the one developed in [13]. Finally, we present a range of numerical tests to demonstrate the improvements due to the proposed polar treatment. In the end, we summarize the implications of the proposed treatments and conclude by giving some hints for the treatment of the other singular points that arise in meshes aligned with the flux surfaces.

2 bi-cubic Hermite Bézier FEM

We consider the numerical approximation of a system of time-dependent partial differential equations (PDEs) using FEM. The physical problem of interest is the plasma flows inside a tokamak which has cylindrical symmetry. Therefore, the governing equations are written in the cylindrical coordinate system (R, Z, ϕ) where ϕ denotes periodic toroidal direction and the

poloidal plane is expressed in terms of the coordinates $\boldsymbol{\xi} := (R, Z)^{\mathrm{T}}$. The choice of the coordinate system also allows the use of an efficient Fourier spectral method for the discretization in ϕ direction. In any poloidal plane section $\Omega_{\boldsymbol{\xi}}$ defined by the coordinates $\boldsymbol{\xi}$ the plasma is mostly confined to the concentric closed magnetic flux surfaces. Since the plasma dynamics is constrained to these flux surfaces it is useful to device the numerical approximation in $\Omega_{\boldsymbol{\xi}}$ with the geometrical grids that are aligned to the magnetic flux iso-surfaces.

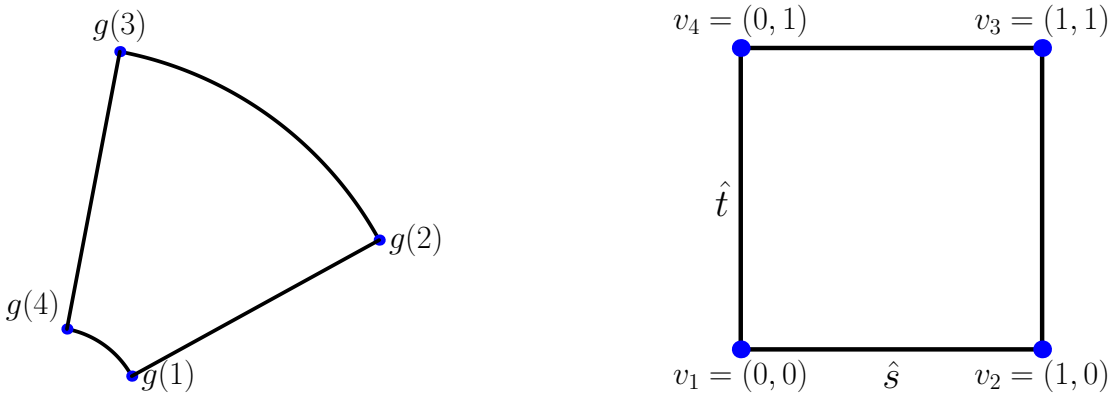

(a) (b)

Figure 2: a) A curved element Ω_e in the poloidal plane. b) The bi-unit reference element $\hat{\tau}$.

We focus on the part of the problem associated to the bicubic Hermite Bézier FEM applied in the poloidal plane and hence we express the strong form of PDE in $\Omega_{\boldsymbol{\xi}}$ that governs the space-time evolution of a function $\boldsymbol{w}(t, \boldsymbol{\xi})$ for $t \in [0, T]$ and $\boldsymbol{\xi}$ in $\Omega \subset \mathbb{R}^2$. The strong form of a PDE is compactly written in the residual form as:

$$\mathcal{R}(\boldsymbol{w}) = 0 \qquad \text{where} \qquad \mathcal{R}(\boldsymbol{w}) := \frac{\partial \boldsymbol{w}}{\partial t} + \mathcal{L}\boldsymbol{w} - \boldsymbol{f} \tag{1}$$

where $\mathcal{R}$ represents the residual, $\mathcal{L}$ the differential operator and $\boldsymbol{f} := \boldsymbol{f}(\boldsymbol{w}, \boldsymbol{\xi})$ the source term. The Galerkin weak form for the above problem can be written as: Find $\boldsymbol{w} \in [0, T] \times \boldsymbol{\mathcal{V}}(\Omega_{\boldsymbol{\xi}})$ such that for any $\boldsymbol{w}^* \in \boldsymbol{\mathcal{V}}(\Omega_{\boldsymbol{\xi}})$:

$$\int_{\Omega_{\boldsymbol{\xi}}} \boldsymbol{w}^* \cdot \mathcal{R}(\boldsymbol{w})\, d\boldsymbol{\xi} = 0 \tag{2}$$

where $\boldsymbol{w}^*$ are test functions in a suitable Hilbert space $\boldsymbol{\mathcal{V}}$. We consider the mapping of a parametric space $\boldsymbol{\zeta}$ to the physical space $\Omega_{\boldsymbol{\xi}}$. Let $\boldsymbol{\zeta} := (\mathrm{s}, \mathrm{t})^{\mathrm{T}}$ denote the coordinates of a point in the parametric space, then the mapping is written as:

$$\boldsymbol{\xi} := \boldsymbol{\xi}(\mathrm{s}, \mathrm{t}) \qquad \text{and inversely} \qquad \boldsymbol{\zeta} := \boldsymbol{\zeta}(R, Z) \tag{3}$$

The parametric domain $\boldsymbol{\zeta}$ is decomposed into non-overlapping rectangular elements τ_ℓ such that $\boldsymbol{\zeta} = \bigcup_{\ell=1}^{\mathrm{N_e}} \tau_\ell$ where $\mathrm{N_e}$ is the total number of elements. The approximated physical space $\Omega_{\boldsymbol{\xi}_h}$ is obtained by the mapping of $\boldsymbol{\zeta}$ formulated in a smooth finite element space. In general, this transformation is applied on a domain with no singularity. In the bicubic Hermite-Bézier FEM

the isoparametric mapping maps a rectangular element τ_ℓ in $\boldsymbol{\zeta}$ onto a curved quadrangle Ω_e in $\Omega_{\boldsymbol{\xi}_h}$ (see Figure 2a). On any element τ_ℓ a scalar function $f(\boldsymbol{\zeta})$, restricted to τ_ℓ, is represented in terms of the basis functions with four coefficients at each vertex $g(v)$, where v (= 1 to 4) is the local vertex numbering in any element and $g(v)$ denotes the global vertex number in a grid. These coefficients are the value of that function, its first order derivatives and the cross derivative at that vertex:

$$f_{g(v),1} = f\left(\boldsymbol{\zeta}_{g(v)}\right), \qquad f_{g(v),2} = \frac{\partial f}{\partial \mathrm{s}}\left(\boldsymbol{\zeta}_{g(v)}\right), \qquad f_{g(v),3} = \frac{\partial f}{\partial \mathrm{t}}\left(\boldsymbol{\zeta}_{g(v)}\right), \qquad f_{g(v),4} = \frac{\partial^2 f}{\partial \mathrm{s}\partial \mathrm{t}}\left(\boldsymbol{\zeta}_{g(v)}\right)$$

The coefficients above are equivalent to those in the Hermite interpolation. The Hermite FEM is a special case of bicubic Hermite Bézier FEM [16]. Each element τ_ℓ is also mapped onto the bi-unit reference element $\hat{\tau}(\hat{s},\hat{t}) = [0,1]\times[0,1]$ (see Figure 2b). The mapping from any τ_ℓ to $\hat{\tau}$ is constructed such that $\mathrm{s} = \mathrm{s}(\hat{s})$ and $\mathrm{t} = \mathrm{t}(\hat{t})$ and the coefficients to represent a function $f(\tau(\hat{\tau})) = \hat{f}(\hat{\tau})$ are written as:

$$\begin{aligned}
\hat{f}_{v,1} &= \hat{f}\big|_v = f_{g(v),1} \\
\hat{f}_{v,2} &= \left.\frac{\partial \hat{f}}{\partial \hat{s}}\right|_v = \left.\frac{\partial f}{\partial \mathrm{s}}\frac{d\mathrm{s}}{d\hat{s}}\right|_v = f_{g(v),2}\left.\frac{d\mathrm{s}}{d\hat{s}}\right|_v \\
\hat{f}_{v,3} &= \left.\frac{\partial \hat{f}}{\partial \hat{t}}\right|_v = \left.\frac{\partial f}{\partial \mathrm{t}}\frac{d\mathrm{t}}{d\hat{t}}\right|_v = f_{g(v),3}\left.\frac{d\mathrm{t}}{d\hat{t}}\right|_v \\
\hat{f}_{v,4} &= \left.\frac{\partial^2 \hat{f}}{\partial \hat{s}\partial \hat{t}}\right|_v = \left.\frac{\partial^2 f}{\partial \mathrm{s}\partial \mathrm{t}}\,\frac{d\mathrm{s}}{d\hat{s}}\right|_v \left.\frac{d\mathrm{t}}{d\hat{t}}\right|_v = f_{g(v),4}\left.\frac{d\mathrm{s}}{d\hat{s}}\right|_v \left.\frac{d\mathrm{t}}{d\hat{t}}\right|_v
\end{aligned}$$

where the coefficients $\hat{f}_{v,d}$ with $d = 1,2,3,4$ are the Hermite data associated to $\hat{f}(\hat{\tau})$. The terms $d\mathrm{s}/d\hat{s}$ and $d\mathrm{t}/d\hat{t}$ at a vertex v, called as scale factors, arise due to the mapping from parametric to reference element and can be different in all the four elements sharing that vertex v. For clarity, we rewrite the relations between the coefficients for a function f in τ_l and $\hat{\tau}$ as:

$$\hat{f}_{v,1} = f_{g(v),1}\ \sigma^e_{v,1}, \quad \hat{f}_{v,2} = f_{g(v),2}\ \sigma^e_{v,2}, \quad \hat{f}_{v,3} = f_{g(v),3}\ \sigma^e_{v,3}, \quad \hat{f}_{v,4} = f_{g(v),4}\ \sigma^e_{v,4} \tag{4}$$

where, $\sigma^e_{v,1} = 1$; $\sigma^e_{v,2}$ and $\sigma^e_{v,3}$ take the values $d\mathrm{s}/d\hat{s}$ and $d\mathrm{t}/d\hat{t}$ which are different in each element τ_l sharing the vertex v, while $\sigma^e_{v,4} = \sigma^e_{v,2}\ \sigma^e_{v,3}$. These scale factors $\sigma^e_{v,d}$ arrange G^1 regularity across the elements in the parametric space and consequently C^1 regularity in the physical space. Using the relations (4), the interpolation of a function $\hat{f}(\hat{\tau})$ on the reference element is written as:

$$\hat{f}(\hat{s},\hat{t}) = \sum_{v=1}^{4}\sum_{d=1}^{4} \hat{f}_{v,d}\ B_{v,d}(\hat{s},\hat{t}) = \sum_{v=1}^{4}\sum_{d=1}^{4} f_{g(v),d}\ \sigma^e_{v,d}\ B_{v,d}(\hat{s},\hat{t}) \qquad 0 \le \hat{s},\hat{t} \le 1$$

where the index d denotes the degrees of freedom and the index v denotes the vertices. In the isoparametric framework, the above interpolation is used to write the geometric mapping of the grid coordinates in terms of the bi-cubic Bézier basis function $B_{v,d}\left(\hat{s},\hat{t}\right)$ on $\hat{\tau}$ as:

$$\boldsymbol{\xi}^e_h(\hat{s},\hat{t}) = \sum_{v=1}^{4}\sum_{d=1}^{4} \boldsymbol{\xi}_{g(v),d}\ \sigma^e_{v,d}\ B_{v,d}(\hat{s},\hat{t}) \qquad 0 \le \hat{s},\hat{t} \le 1 \tag{5}$$

The coefficients $\boldsymbol{\xi}_{g(v),d}$ are the properties of the vertex (nodal formulation) which all the elements containing that vertex share. The scale factors $\sigma^e_{v,d}$ are the properties of the elements and are

constant on each element. The four basis functions associated with the first vertex of the reference element $\hat{\tau}$ (see Figure (2b)) are written below:

$$\begin{aligned} B_{1,1}(\hat{s},\hat{t}) &= (1-\hat{s})^2(1-\hat{t})^2(1+2\hat{s})(1+2\hat{t}) \\ B_{1,2}(\hat{s},\hat{t}) &= 3(1-\hat{s})^2(1-\hat{t})^2(1+2\hat{t})\hat{s} \\ B_{1,3}(\hat{s},\hat{t}) &= 3(1-\hat{s})^2(1-\hat{t})^2(1+2\hat{s})\hat{t} \\ B_{1,4}(\hat{s},\hat{t}) &= 9(1-\hat{s})^2(1-\hat{t})^2\hat{s}\ \hat{t} \end{aligned}$$

The basis functions associated with the other vertices can be obtained by replacing $\hat{s} \to 1-\hat{s}$ and/or $\hat{t} \to 1-\hat{t}$ depending upon the vertex number [26]. The grid generation consists of computing the coefficients $\boldsymbol{\xi}_{g(v),d}$ and $\sigma^e_{v,d}$ such that the image of the parametric domain describes the physical domain up to the accuracy of the numerical approximation. Any circular or non-circular polar grid can be constructed based on the mapping described above. Computation of the mapping parameters is not always easy, especially for the grid blocks aligned to the magnetic flux iso-surfaces [22]. For our purpose, we will assume that the polar grid constructed using the mapping is available to us and the parameters $\boldsymbol{\xi}_{g(v),d}$ and $\sigma^e_{v,d}$ are known.

The Galerkin FEM formulation for weak form of the PDE is written as: Find $\boldsymbol{w}_h \in [0,T] \times \boldsymbol{\mathcal{V}}_h\left(\Omega_{\boldsymbol{\xi}_h}\right)$ such that for any $\boldsymbol{w}^\star \in \boldsymbol{\mathcal{V}}_h\left(\Omega_{\boldsymbol{\xi}_h}\right)$:

$$\int_{\Omega_{\boldsymbol{\xi}_h}} \boldsymbol{w}^\star \cdot \mathcal{R}(\boldsymbol{w}_h)\, d\boldsymbol{\xi} = 0 \tag{6}$$

where $\boldsymbol{w}^\star$ are the test functions, $\boldsymbol{\mathcal{V}}_h\left(\Omega_{\boldsymbol{\xi}_h}\right)$ is the space of the trial functions defined over discretized domain $\Omega_{\boldsymbol{\xi}_h}$. In practice the integral (6) may be reformulated by applying integration by parts to reduce the order of derivatives in the equations. The Galerkin FEM gives the central numerical approximation which may generate the spurious oscillations when the dynamics is convection-dominated. Therefore, the additional contribution coming from Taylor-Galerkin stabilization method is added to the integral to enforce the numerical stability.

In the bi-cubic Hermite-Bézier FEM the restriction of $\boldsymbol{w}_h$ on any element Ω_e is written as:

$$\boldsymbol{w}^e_h(\boldsymbol{\xi}) = \hat{\boldsymbol{w}}^e_h\left(\hat{s}\left(\boldsymbol{\xi}\right), \hat{t}\left(\boldsymbol{\xi}\right)\right) \quad \text{where} \quad \hat{\boldsymbol{w}}^e_h(\hat{s},\hat{t}) = \sum_{v=1}^{4}\sum_{d=1}^{4} \boldsymbol{w}_{g(v),d}\ \sigma^e_{v,d}\ B_{v,d}(\hat{s},\hat{t}) \qquad 0 \le \hat{s},\hat{t} \le 1 \tag{7}$$

The coefficients $\boldsymbol{w}_{g(v),d}$ are the degrees of freedom defining the approximated function $\boldsymbol{w}_h(\boldsymbol{\xi})$ and are the unknowns of the discrete problem. A link between the $\boldsymbol{w}_{g(v),d}$ and the derivatives of the function in the reference element is given by the change of variables. For any scalar function $\mathcal{W}\left(\boldsymbol{\xi}(\tau(\hat{\tau}))\right) = W\left(\hat{\tau}\right)$ the following relations can be written:

$$W = \mathcal{W} \tag{8}$$

$$\frac{\partial W}{\partial \hat{s}} = \nabla_{\boldsymbol{\xi}}\mathcal{W} \cdot \frac{\partial \boldsymbol{\xi}}{\partial \hat{s}} \tag{9}$$

$$\frac{\partial W}{\partial \hat{t}} = \nabla_{\boldsymbol{\xi}}\mathcal{W} \cdot \frac{\partial \boldsymbol{\xi}}{\partial \hat{t}} \tag{10}$$

$$\frac{\partial^2 W}{\partial \hat{s}\partial \hat{t}} = \nabla_{\boldsymbol{\xi}}\mathcal{W} \cdot \frac{\partial^2 \boldsymbol{\xi}}{\partial \hat{s}\partial \hat{t}} + \mathcal{H}_{\boldsymbol{\xi}}\left(\mathcal{W}\right) : \left(\frac{\partial \boldsymbol{\xi}}{\partial \hat{s}} \otimes \frac{\partial \boldsymbol{\xi}}{\partial \hat{t}}\right) \tag{11}$$

where $\mathcal{H}_{\boldsymbol{\xi}}(\mathcal{W})$ is the Hessian matrix in the physical space and the partial derivatives $\frac{\partial \boldsymbol{\xi}}{\partial \hat{s}}$, $\frac{\partial \boldsymbol{\xi}}{\partial \hat{t}}$ and $\frac{\partial^2 \boldsymbol{\xi}}{\partial \hat{s}\partial \hat{t}}$ are computed using the scale factors. The relations (8)-(11) will be useful afterwards

to develop a simple, efficient and accurate strategy for the polar grid center that enforces the regularity of functions in the physical space.

3 Singularity at the Polar grid center

Let us consider an annular grid with curved quadrangular elements constructed using bi-cubic Hermite Bézier formulation with its inner boundary at a distance $\varepsilon \ll 1$ from the geometrical center (see Figure 3). Let us denote by N_θ the number of vertices located at the distance ε. In the limit $\varepsilon \to 0$, an annular grid becomes a polar grid, all N_θ vertices collapse to the geometrical grid center and the geometrical transformation from the parametric to physical space becomes singular. At this limit, the curved quadrangular elements degenerate to the triangular elements as one of the edges that falls on the grid center collapses to a point. Since N_θ points fall at the geometrical center, there are $4N_\theta$ independent degrees of freedom at the polar grid center together.

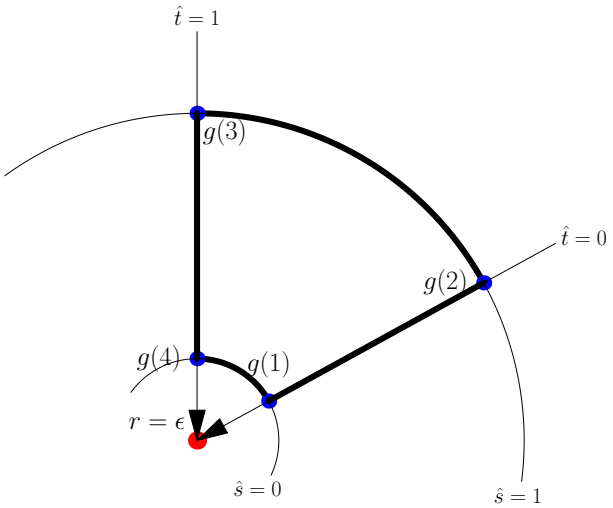

Figure 3: An element Ω_e on the polar grid center: As radius $r \to 0$, the edge formed by $g(1)$ and $g(4)$ collapses to a point which is the polar grid center.

Figure (4a)-(4d) shows the overlapped global shape functions at the polar grid center associated with the four degrees of freedom respectively. It can be seen that the third and fourth basis functions form oscillatory shape functions in the azimuthal direction and may give an oscillatory approximation of a smooth function near the polar grid center. The bi-cubic Hermite Bézier FEM does not even ensure the continuity of the functions at the grid center and the accuracy of the FEM is lost at the grid center. The polar grid center then can act as a source of spurious oscillations and can pollute the numerical solution. The numerical noise at the polar grid center may remain bounded when a physical or numerical model is diffusion-dominated. For the hyperbolic equations, however, the polar grid center can severely restrict the stability and the accuracy of the numerical method. Therefore, proper treatment of the polar grid center is needed.

In practice, a crude way is used to cure the numerical problems at the polar grid center by enforcing C^0 regularity. In this treatment the degrees of freedom $\boldsymbol{w}_{g(v),1}$ at the polar grid center are shared, $\boldsymbol{w}_{g(v),3}$ are enforced to zero while $\boldsymbol{w}_{g(v),2}$ and $\boldsymbol{w}_{g(v),4}$ are kept free. This C^0

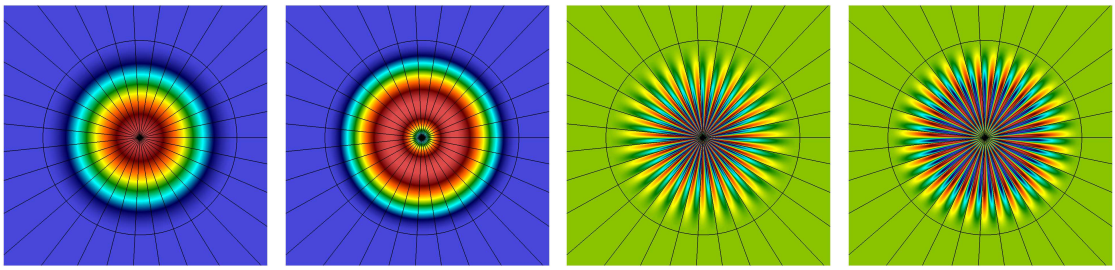

(a) (b) (c) (d)

Figure 4: Plots of the global shape functions associated with (a) $W_{g(v),1}$ (b) $W_{g(v),2}$ (c) $W_{g(v),3}$ and (d) $W_{g(v),4}$ overlapped at the polar grid center.

polar treatment has been used so far with success in most numerical simulations. Another polar treatment used in practice enforces $\boldsymbol{w}_{g(v),4}$ to zero at the polar grid center. This polar treatment is used in addition to C^0 treatment and we refer to it as the 'intermediate polar treatment'. It removes the contribution due to the third and fourth basis functions from the interpolation and thereby reduces the accuracy of the interpolation on the elements on the polar grid. Sometimes hyperdiffusive terms localized around the polar grid center are used to run the simulations in a numerically stable way, which can be an unelegant but acceptable solution for instabilities at the plasma edge. In the case of the plasma core instabilities, however, such localized use of the hyperdiffusive terms alter their physical behavior. Below, we develop a mathematically consistent polar grid treatment that enforces the C^1 regularity in the physical space, and at the same time, it preserves the accuracy of the interpolation.

To analyze the problem at the polar grid center we look at the asymptotic limit $\epsilon \to 0$ at which an element Ω_e falls onto the grid center (see Figure (3)). For the discussion, let us assume that the curved edge connecting the vertices $g(1)$ and $g(4)$ of an element Ω_e falls on the polar grid center as shown in Figure (3). In the reference element $\hat{\tau}$, this curved edge maps onto $\hat{s} = 0$ and therefore we examine the trace of $\boldsymbol{\xi}$ and its derivatives along $\hat{s} = 0$. The interpolation for $\boldsymbol{\xi}(\hat{s}, \hat{t})$ is written below at $\hat{s} = 0$:

$$\begin{aligned}\boldsymbol{\xi}(0,\hat{t}) = \boldsymbol{\xi}_{g(1),1}\ \sigma^e_{1,1}\ B_{1,1}(0,\hat{t}) + \boldsymbol{\xi}_{g(1),3}\ \sigma^e_{1,3}\ B_{1,3}(0,\hat{t}) \\ + \boldsymbol{\xi}_{g(4),1}\ \sigma^e_{4,1}\ B_{4,1}(0,\hat{t}) + \boldsymbol{\xi}_{g(4),3}\ \sigma^e_{4,3}\ B_{4,3}(0,\hat{t})\end{aligned} \tag{12}$$

In above relations, out of 16 only 4 terms contribute to the interpolation and others vanish at $\hat{s} = 0$. By construction of the bi-cubic Bézier FEM, we have $\sigma^e_{1,1} = \sigma^e_{4,1} = 1$. Further, it is easy to see the partition of unity at $\hat{s} = 0$:

$$B_{1,1}(0,\hat{t}) + B_{4,1}(0,\hat{t}) = 1 \tag{13}$$

which can be used in equation (12) to obtain:

$$\boldsymbol{\xi}\left(0,\hat{t}\right) = \boldsymbol{\xi}_{g(4),1} + \left(\boldsymbol{\xi}_{g(1),1} - \boldsymbol{\xi}_{g(4),1}\right)\ B_{1,1}(0,\hat{t}) + \boldsymbol{\xi}_{g(1),3}\ \sigma^e_{1,3}\ B_{1,3}(0,\hat{t}) + \boldsymbol{\xi}_{g(4),3}\ \sigma^e_{4,3}\ B_{4,3}(0,\hat{t})$$

Asymptotically when $\varepsilon \to 0$, the curve $\boldsymbol{\xi}\left(0,\hat{t}\right)$ collapses to the position of the polar grid center $\boldsymbol{\xi}_0$ which is independent of the parametric coordinate $\hat{t}$. Therefore we can deduce that:

$$\boldsymbol{\xi}_{g(1),1} = \boldsymbol{\xi}_{g(4),1} = \boldsymbol{\xi}_0, \qquad \boldsymbol{\xi}_{g(1),3} = 0 \qquad \text{and} \qquad \boldsymbol{\xi}_{g(4),3} = 0. \tag{14}$$

Using the above relations and the $\hat{t}$ derivative of the equation (13) it is easy to see that:

$$\frac{\partial \boldsymbol{\xi}}{\partial \hat{t}}\left(0,\hat{t}\right) = 0 \tag{15}$$

A similar analysis for the interpolation of a scalar function $W(\hat{s},\hat{t})$ at $\hat{s}=0$ gives:

$$W_{g(1),1} = W_{g(4),1} = W_0, \qquad W_{g(1),3} = 0, \qquad W_{g(4),3} = 0 \qquad \text{and} \qquad \frac{\partial W}{\partial \hat{t}}\left(0,\hat{t}\right) = 0 \tag{16}$$

where W_0 is the value of the function at the polar grid center. The first of the above relation implies that the first degrees of freedom associated with the two vertices falling onto the grid center must have a common value. The last relation removes the third degrees of freedom and hence the variation in the azimuthal direction from the interpolation. These are the relations on which the C^0 polar treatment is based upon.

To achieve C^1 regularity at the polar grid center, we now look at the second and fourth degrees of freedom at the polar grid center which are associated to $\hat{s}$ and mixed derivatives of a function W. The relation (15) can be used in the equations (8)-(11) to rewrite the relations between derivatives in the reference element and the physical space at the polar grid center as:

$$W_v = \mathcal{W}\left(\boldsymbol{\xi}_0\right) \tag{17}$$

$$\left.\frac{\partial W}{\partial \hat{s}}\right|_v = \nabla_{\boldsymbol{\xi}}\mathcal{W}\left(\boldsymbol{\xi}_0\right)\cdot\left.\frac{\partial \boldsymbol{\xi}}{\partial \hat{s}}\right|_v \tag{18}$$

$$\left.\frac{\partial W}{\partial \hat{t}}\right|_v = \nabla_{\boldsymbol{\xi}}\mathcal{W}\left(\boldsymbol{\xi}_0\right)\cdot\left.\frac{\partial \boldsymbol{\xi}}{\partial \hat{t}}\right|_v = 0 \tag{19}$$

$$\left.\frac{\partial^2 W}{\partial \hat{s}\partial \hat{t}}\right|_v = \nabla_{\boldsymbol{\xi}}\mathcal{W}\left(\boldsymbol{\xi}_0\right)\cdot\left.\frac{\partial^2 \boldsymbol{\xi}}{\partial \hat{s}\partial \hat{t}}\right|_v \tag{20}$$

The above relations express all the degrees of freedom associated to the polar grid center in terms of the three quantities: the value of function $\mathcal{W}\left(t,\boldsymbol{\xi}_0\right)$ and its gradient $\nabla_{\boldsymbol{\xi}}\mathcal{W}\left(t,\boldsymbol{\xi}_0\right)$ in the physical space at the polar grid center. Indeed, these relations should be satisfied at all the vertices $g(v)$ that collapse on the polar grid center. Therefore we propose a polar treatment in which we apply the relations (17)-(20) at all the vertices on the grid center. Compactly, they can be written as the transformation of the quantities from the reference element to the physical space as:

$$\boldsymbol{W}\big|_{g(v)} = \mathbb{T}^e\big|_{g(v)}\,\boldsymbol{\mathcal{W}}\big|_{\boldsymbol{\xi}=\boldsymbol{\xi}_0} \tag{21}$$

where

$$\boldsymbol{W}\big|_{g(v)} = \begin{pmatrix} W \\ \frac{\partial W}{\partial \hat{s}} \\ \frac{\partial^2 W}{\partial \hat{s}\partial \hat{t}} \end{pmatrix}, \quad \boldsymbol{\mathcal{W}}\big|_{g(v)} = \begin{pmatrix} \mathcal{W} \\ \frac{\partial \mathcal{W}}{\partial R} \\ \frac{\partial \mathcal{W}}{\partial Z} \end{pmatrix} \quad \text{and} \quad \mathbb{T}^e\big|_{g(v)} = \begin{pmatrix} 1 & 0 & 0 \\ 0 & \frac{\partial R}{\partial \hat{s}} & \frac{\partial Z}{\partial \hat{s}} \\ 0 & \frac{\partial^2 R}{\partial \hat{s}\partial \hat{t}} & \frac{\partial^2 Z}{\partial \hat{s}\partial \hat{t}} \end{pmatrix}$$

Equation (21) can be thought as a transformation from the old to the new degrees of freedom where the latter are $\mathcal{W}\left(t,\boldsymbol{\xi}_0\right)$, $\frac{\partial \mathcal{W}}{\partial R}\left(t,\boldsymbol{\xi}_0\right)$ and $\frac{\partial \mathcal{W}}{\partial Z}\left(t,\boldsymbol{\xi}_0\right)$. The transformation matrix $\mathbb{T}^e\big|_{g(v)}$ is different for the each vertex collapsing on the grid center, however the new degrees of freedom are common for the each vertex. This leads to the formulation of the problem in terms of the unique value of the function $\mathcal{W}$ and its derivatives at the polar grid center.

The use of the new degrees of freedom requires the basis functions in the interpolation to change accordingly. Using equation (7), the interpolation of a scalar function $W(\hat{\tau})$ restricted to $\hat{s} = 0$ is re-written below and then written in terms of the new basis functions as:

$$W(0,\hat{t}) = \sum_{v=1}^{4} \tilde{\boldsymbol{B}}^e_{g(v)}(0,\hat{t}) \cdot \tilde{\boldsymbol{W}}_{g(v)} = \sum_{v=1}^{4} \boldsymbol{N}^e_{g(v)}(0,\hat{t}) \cdot \boldsymbol{\mathcal{W}}(\boldsymbol{\xi}_0)$$

where the index v denotes the vertex of an element, $\tilde{\boldsymbol{B}}^e_{g(v)} = \left(\sigma^e_{v,1}\ B_{v,1},\ \sigma^e_{v,2}\ B_{v,2},\ \sigma^e_{v,4}\ B_{v,4}\right)^T$ is the vector containing basis functions and the vector $\tilde{\boldsymbol{W}}_{g(v)} = \left(W,\ \partial_{\hat{s}}W,\ \partial_{\hat{s}\hat{t}}W\right)^T|_{g(v)}$ denotes the associated degrees of freedom. We recall here that the degree of freedom $\partial_{\hat{t}}W = 0$ in the limit $\hat{s} \to 0$. The vector of new basis functions is given by

$$\boldsymbol{N}^e_{g(v)} = \left[\mathbb{T}^e|_{g(v)}\right]^{\mathrm{T}}\ \tilde{\boldsymbol{B}}^e_{g(v)} \tag{22}$$

and the associated new degrees of freedom are $\boldsymbol{\mathcal{W}}(\boldsymbol{\xi}_0)$. For a typical polar grid, the three global shape functions $\mathcal{N}_1(\boldsymbol{\xi})$, $\mathcal{N}_2(\boldsymbol{\xi})$ and $\mathcal{N}_3(\boldsymbol{\xi})$ obtained by overlapping $\boldsymbol{N}^e_{g(1)}$, $\boldsymbol{N}^e_{g(2)}$ and $\boldsymbol{N}^e_{g(3)}$ respectively for all the vertices on the grid center are shown in Figure (6). These shape functions are associated with the three new unknowns $\mathcal{W}$, $\partial_R\mathcal{W}$ and $\partial_Z\mathcal{W}$ at the grid center respectively. As opposed to the shape functions associated with old degrees of freedom (see Figure (4)), the new shape functions are smooth and continuous in the azimuthal direction.

We now show from a simple numerical test that the new basis functions follow the expected order of convergence. In Figure (5), the L^2-norm of the error in Hermite Bézier interpolation of a smooth function $\mathcal{W}$ computed with the new basis functions is plotted versus element size h. On the circular polar grid, the smooth function is specified as:

$$\mathcal{W} = R^4 + R^3 + R^2 + R + Z^4 + Z^3 + Z^2 + Z$$

The parametric space (r, θ) is assumed to discretized by equispaced points such that the rectangular elements have sides with length:

$$dr = \frac{1}{2^{m+1}}, \qquad d\theta = \frac{2\pi}{2^{m+1}}, \qquad m = 1, 2, ..., 8$$

and $h = \sqrt{dr\ d\theta}$. In Figure (5) it can be seen that the new basis functions preserves the accuracy of the original basis functions. Figure (5) also shows that the reduced order interpolation used in the intermediate polar treatment that converges with the second order accuracy.

Summarizing, the analysis of the interpolation of the grid and physical variables gives an alternate way of writing the interpolation of a function in terms of the new degrees of freedom $\boldsymbol{\mathcal{W}}(\boldsymbol{\xi}_0)$ and basis functions $\boldsymbol{N}^e_{g(v)}$. There are three new degrees of freedom at the polar grid center: the value of a function $\mathcal{W}$ and its gradient $\nabla\mathcal{W}$ at the polar grid center. Therefore, we have three unknowns associated with the polar grid center. The new basis functions $\boldsymbol{N}^e_{g(v)}$ are simply the linear transformation given by equation (22) of the old basis functions. The superscript e highlights that the new basis functions are different in each element falling on the grid center. The transformation (22) is to be applied only at the vertices falling onto the polar grid center in each element and leaving all other vertices untouched.

The polar grid center treatment we have developed above uses the smooth basis functions that preserve the accuracy of the interpolation and enforces C^1 continuity directly in the physical space. The implementation of the proposed polar treatment is straightforward and amounts to the application of the transformation (22) on the bi-cubic Hermite Bézier basis functions associated with the vertices on the polar grid center. The rest of the numerical algorithm remains unchanged while the linear system (formed due to finite element discretization of equation (6)) solves for the new degrees of freedom at the grid center.

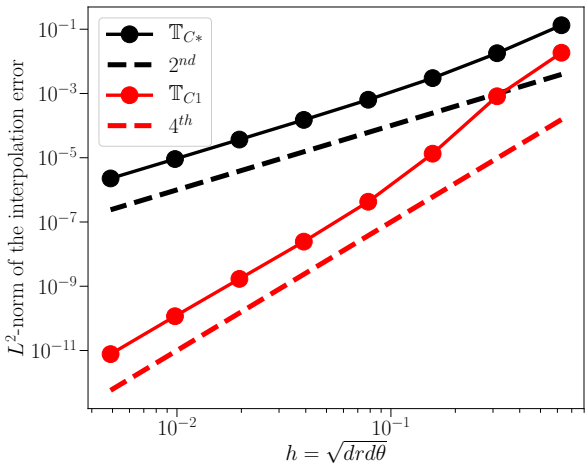

Figure 5: L^2-norm of the interpolation error for the function $\mathcal{W} = R^4 + R^3 + R^2 + R + Z^4 + Z^3 + Z^2 + Z$ plotted vs element size h in case of the intermediate ($\mathbb{T}_{C*}$) and C^1 ($\mathbb{T}_{C1}$) polar treatment.

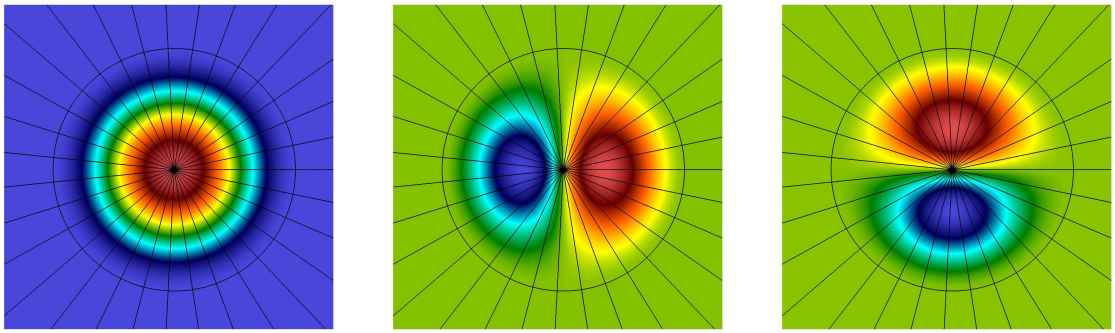

(a) $\mathcal{N}_1(\boldsymbol{\xi})$ (b) $\mathcal{N}_2(\boldsymbol{\xi})$ (c) $\mathcal{N}_4(\boldsymbol{\xi})$

Figure 6: The new global shape functions plotted at the polar grid center that are associated with the new degrees of freedom: (a) $\mathcal{W}_0$ (b) $\partial_R \mathcal{W}$ and (c) $\partial_Z \mathcal{W}$

Note:

The C^1 polar treatment developed here has some similarities with the case $k = 1$ of the generalized work to construct C^k smooth polar splines presented in [13]. In both constructions, three basis functions are constructed at the polar center which are a linear combination of the underlying basis functions. While the linear combination turns out naturally in this work, an 'extraction operator' $\bar{\boldsymbol{E}}^1$ provides the required linear combination in [13] to enforce C^1 continuity. This operator is constructed using 'triangular Bernstein polynomials' as the basis functions on a triangular domain satisfying the Hermite data at the polar point. This triangular domain needs to encompass the polar point and can be entirely arbitrary however, the authors in [13] provide

an option (for standardization) that gives the following triangular Bernstein polynomials:

$$
\begin{aligned}
T_1 &= \frac{1}{3} + \frac{2R}{3\tau_1} \\
T_2 &= \frac{1}{3} - \frac{R}{\tau_1} + \frac{\sqrt{3}Z}{\tau_1} \\
T_3 &= \frac{1}{3} - \frac{R}{\tau_1} - \frac{\sqrt{3}Z}{\tau_1}
\end{aligned}
$$

An estimate for τ_1 is also given in [13] which guarantees non-negative extraction coefficients $\bar{\boldsymbol{E}}^1$. The equivalent functions $\widetilde{T}_1$, $\widetilde{T}_2$ and $\widetilde{T}_3$ provided by the C^1 polar treatment proposed here turn out to be:

$$
\begin{aligned}
\widetilde{T}_1 &= 1 = T_1 + T_2 + T_3 \\
\widetilde{T}_2 &= R = \frac{\tau_1}{2}\left(2 - 3T_2 - 3T_3\right) \\
\widetilde{T}_3 &= Z = \frac{\sqrt{3}\tau_1}{2}\left(T_2 - T_3\right)
\end{aligned}
$$

The polar treatment in [13] requires defining a triangular domain around the polar center which is not needed in our development. Indeed the basis functions we construct are already associated with the Hermite data [16].

4 Numerical results

In this section, we present the numerical tests performed on the linear model problems and MHD instabilities to compare the performance of the three polar treatments. For the sake of the discussion, we identify four different situations based on the transformations to be applied on the basis functions at the polar grid center.

1) No polar treatment ($\mathbb{T}^e_{g(v)} = \mathbb{I}$) : The identity transformation denotes the use of original formulation and hence no special treatment at the polar treatment.

2) C^0 polar treatment ($\mathbb{T}^e_{g(v)} = \mathbb{T}_{C0}$) : The transformation to enforce the C^0 regularity at the polar grid center by using the relations (16).

3) Intermediate polar treatment ($\mathbb{T}^e_{g(v)} = \mathbb{T}_{C*}$) : In addition to the above C^0 polar treatment the order of the interpolation is reduced by removing the contribution of the fourth basis functions from the interpolation.

4) C^1 polar treatment ($\mathbb{T}^e_{g(v)} = \mathbb{T}_{C1}$) : The transformation developed in Section above to enforce the C^1 regularity at the polar grid center.

4.1 Linear model problems

4.1.1 Poisson's equation

First we consider a linear elliptic PDE and use the bi-cubic Hermite Bézier FEM to compute the numerical solution on the series of polar grids. Poisson's equation on the unit disc is written with the boundary conditions as:

$$-\nabla^2 u = 1 \qquad \forall \boldsymbol{\xi} \in \Omega \tag{23}$$

$$u = 0 \qquad \forall \boldsymbol{\xi} \in \partial\Omega \tag{24}$$

The exact solution for this equation is given by $u_{ex}(\boldsymbol{\xi}) = (1 - R^2 - Z^2)/4$. The domain on the unit disk Ω is discretized using bi-cubic Hermite Bézier formulation to construct a polar grid with N_r and N_θ points in the radial and azimuthal direction respectively. The system of linear equations resulting due to the discretization is solved exactly using LAPACK [27] library. The FEM solver is run on a series of grids with $N_r = N_\theta = 8, 16, 32$ and 64 points with different polar treatments at the polar grid center. Figure (7a) and (7b) shows L^2 and H^1-norm of the error in the numerical solution plotted vs an estimate of the grid size. All the polar treatments used show the negligible difference in the error in the numerical solution of equation (23). The errors follow expected 4^{th} and 3^{rd} order convergence in L^2 and H^1-norm respectively.

4.1.2 Linear advection equation

Next we demonstrate the effect of the polar grid center treatment on a linear hyperbolic PDE. The linear advection equation with the initial condition is written as:

$$\frac{\partial u}{\partial t} + \boldsymbol{c} \cdot \nabla u = 0, \qquad \forall \boldsymbol{\xi} \in \Omega$$

$$u(t = 0, \boldsymbol{\xi}) = u(\boldsymbol{\xi}) = e^{-32[(R-R_c)^2 + (Z-Z_c)^2]}$$

and is solved numerically using the bi-cubic Hermite Bézier FEM on the polar grid with the different polar treatments. The initial condition is specified as Gaussian bump centered around

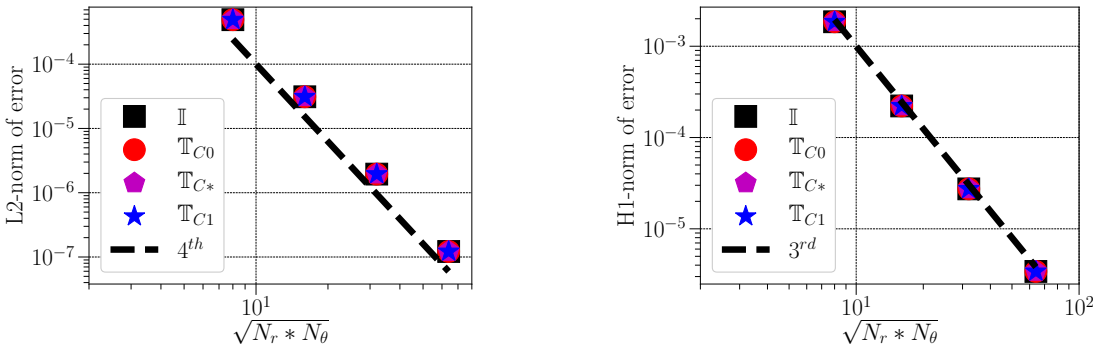

(a) (b)

Figure 7: a) L^2 and b) H^1-norm of the error in the numerical solution of the Poisson's equation plotted vs element size ($\approx \sqrt{N_r * N_\theta}$) where $N_r = N_\theta = 8$, 16, 32 and 64. The different polar treatments considered have negligible difference on the numerical solution.

$R_c = 0.5$ and $Z_c = 0$. The constant vector $\boldsymbol{c} = \{-0.5, 0\}^T$ is chosen such that the initial Gaussian bump advects towards the polar grid center $R = Z = 0$. The time step is specified by the Courant number ($\mathrm{C_C}$):

$$\Delta t_n = \mathrm{C_C}\ \frac{\min\limits_e h_e}{\sqrt{\boldsymbol{c}\cdot\boldsymbol{c}}}$$

where h_e is an estimate for the element size. To estimate h_e approximately, we assume that each element e is formed by linear edges and h_e is taken as the minimum of lengths of two line segments formed by joining midpoints of the linear edges of e. Streamwise Upwind/Petrov-Galerkin stabilization term [28] is added for the numerical stability purposes with the coefficient that is dependent upon the characteristic grid size h_e such that the amount of the stabilization goes to zero as $h_e \to 0$.

Figure (8) shows the evolution of the L^2-norm of the error in the numerical solution of the advection equation computed using explicit Euler's method, with different grids and different polar treatments applied at the polar grid center. Top, middle and bottom rows in Figure (8) show L^2-norm of the error computed on the grids with $N_r = N_\theta = 16$, 32 and 64 respectively, while left and right columns denote the computations with $\mathrm{C_C} = 0.2$ and 0.1 respectively. Without any polar treatment, the simulations blow up at polar grid centers after very few time steps and L^2-norm of the errors becomes unbounded. The application of C^0 polar treatment improves the numerical results at polar grid centers and the errors obtained are bounded for the interval over which simulations are performed. However the simulation with C^0 polar treatment on the finest grid used and $\mathrm{C_C} = 0.2$ blows up after a few time steps due to the numerical instability at the polar grid center. This suggests that grid refinement is not always beneficial when using C^0 treatment. The intermediate polar treatment gives almost identical numerical results to that obtained with C^1 treatment on all grids used here. The linear advection equation is also solved numerically with the implicit Crank-Nicolson method on the series of grids mentioned above. In this case, each polar treatment gives bounded numerical solution even at $\mathrm{C_C} = 10$.

Figure (9) shows the visualizations of the numerical solution computed on the grid with $N_r = N_\theta = 32$, using two different time integration methods and C^1 polar treatment plotted at approximately the same time instant $t \approx 1.3921$. The solution with the explicit Euler's method

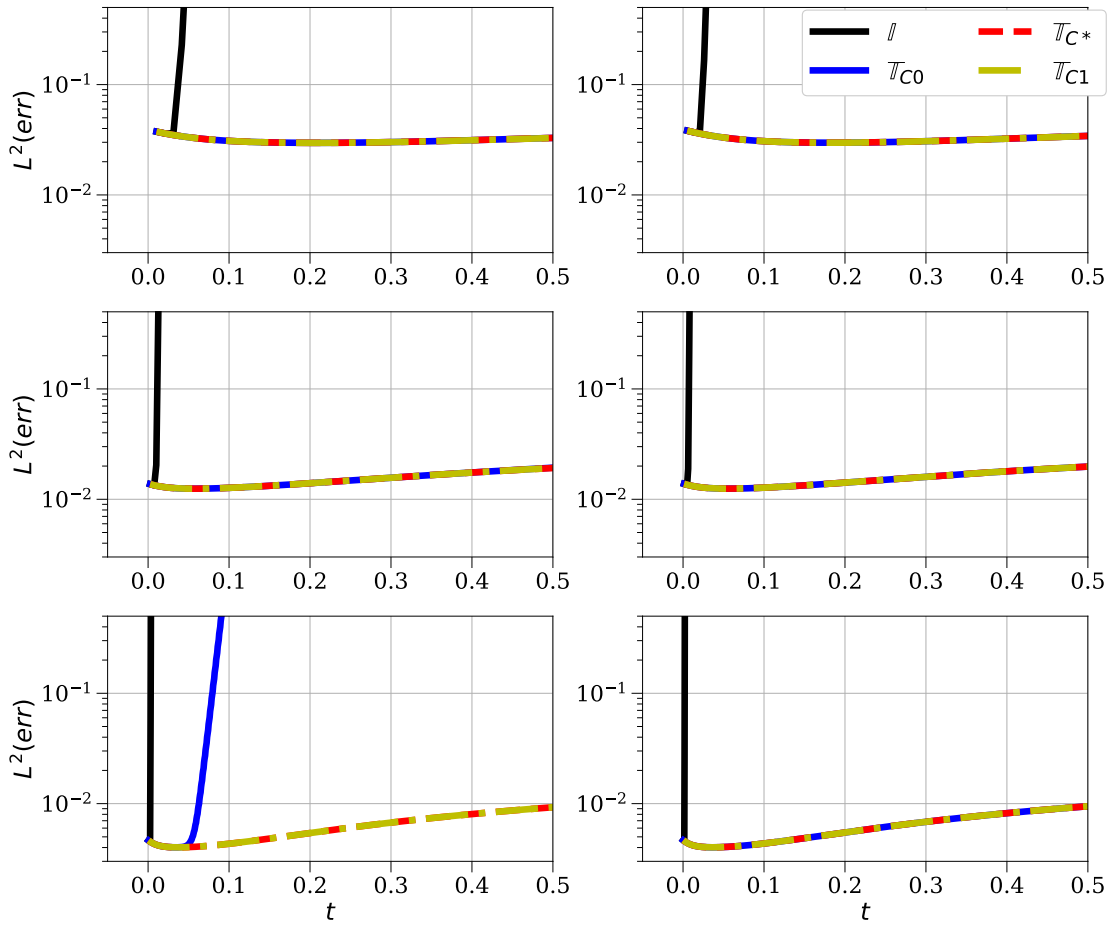

Figure 8: Evolution of the L^2-norm of the error in the numerical solution of the linear advection equation computed using explicit Euler's time integration method. First and second column shows the errors computed using $C_C = 0.2$ and 0.1 respectively while the first, second and third row shows the simulation on the grids with $N_r = N_\theta = 16$, 32 and 64 respectively.

is computed with $C_C = 0.05$ while the solution with the Crank-Nicolson method is computed with $C_C = 1.25$. In both simulations, the Gaussian bump crosses the polar grid center without showing any sign of numerical instabilities. While the explicit Euler method requires smaller time steps to obtain the stable solution at $t \approx 1.3921$, the Crank-Nicolson method gives the stable solution even with C_C=10 (not shown here).

This numerical test with a linear hyperbolic equation suggests that the stability limit at the polar grid center is restrictive for the explicit time integration methods while the implicit methods stabilize the numerical instabilities at the polar grid center.

4.2 MHD instabilities

Finally, we present the numerical tests on MHD equations performed in the computational set-up of JOREK. Fourier representation is used to discretize the MHD equations in the periodic ϕ

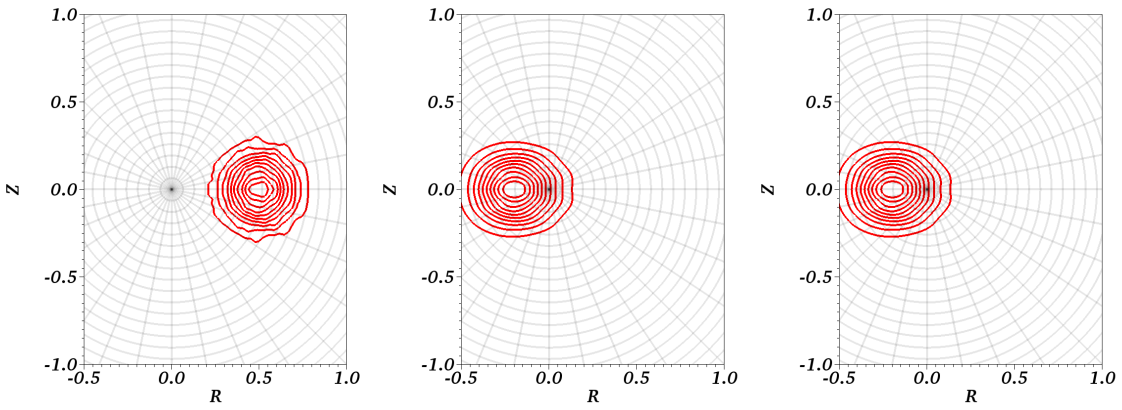

(a) (b) (c)

Figure 9: a) The initial condition for the numerical solution of the linear advection equation on the polar grid with $N_r = N_\theta = 32$. The numerical solution computed with C^1 polar treatment plotted at $t \approx 1.3921$ using b) explicit Euler's method with $\mathrm{C_C} = 0.05$ and c) Crank-Nicolson's method with $\mathrm{C_C} = 1.25$.

direction and n denotes the harmonics in the toroidal direction. In the plane perpendicular to the ϕ direction, called the poloidal plane, the bi-cubic Hermite Bézier FEM is used. Second-order backward difference (Gear's) method [29] is used for the time integration.

In tokamak applications, the investigation of the MHD instabilities is of major interest. The initial condition is chosen as the equilibrium configuration for the ideal MHD equations which is then perturbed by small numbers to evolve the MHD equations in time. The MHD instabilities are mainly of two kinds: current driven and pressure-driven (see 'The Energy Principle' section in Chapter 8 of [30]). The internal kink and tearing modes are examples of current-driven instabilities and they grow around a rational q surface, where q denotes the safety factor of the plasma. Ballooning modes are an example of pressure-driven instabilities and they grow near the location of high-pressure gradients. These instabilities are often investigated for the validation and benchmark of a physical and numerical model for MHD simulation. The growth rates of the magnetic and kinetic energies are often used to quantify these MHD instabilities. In a typical linear run, $n = 0$ mode is kept constant in time and a single $n \neq 0$ is evolved in time. The growth rates are computed during the time interval in which the magnetic and kinetic energies of the perturbations grow exponentially. On the polar grids, however, numerical instabilities may develop at the grid center that can lead to the wrong estimations of the growth rates. In this subsection, we present the linear simulations of the tearing and ballooning modes to highlight the effect of numerical noise at the polar grid center on the estimations of the growth rates. We choose the so-called full MHD equations as the physical model.

Full MHD model

The full MHD model was first implemented and validated for simple geometries in [26] and then it was extended and benchmarked for the realistic geometries in [18]. The visco-resistive full MHD model is written as the system of PDEs for the magnetic vector potential ($\boldsymbol{A}$), plasma

velocity ($\boldsymbol{v}$), density (ρ) and pressure (p) as:

$$\begin{aligned}
&\frac{\partial \boldsymbol{A}}{\partial t} - \boldsymbol{v} \times \boldsymbol{B} = -\eta(\boldsymbol{J} - S_j) \\
&\rho \frac{\partial \boldsymbol{v}}{\partial t} + \rho \boldsymbol{v} \cdot \nabla \boldsymbol{v} + \nabla p - \boldsymbol{J} \times \boldsymbol{B} = \mu \nabla^2 \boldsymbol{v} - \Gamma_\rho \boldsymbol{v} \\
&\frac{\partial \rho}{\partial t} + \nabla \cdot (\rho \boldsymbol{v}) = \nabla \cdot (\mathbb{D} \rho) + S_\rho \\
&\frac{\partial p}{\partial t} + \boldsymbol{v} \cdot \nabla p + \gamma p \nabla \cdot \boldsymbol{v} = \nabla \cdot (\mathbb{K} T) + S_T
\end{aligned}$$

where $\boldsymbol{B}$ denotes the magnetic field and the current is given by $\boldsymbol{J} = \nabla \times \boldsymbol{B}$. The scalar quantities η and μ denote the resistivity and viscosity respectively. The tensors $\mathbb{D}$ and $\mathbb{K}$ denote the anisotropic modeling of the particle diffusion and thermal conductivity respectively. The terms S_j, S_ρ and S_T denote sources while the term Γ_ρ appears due to the non-conservative form of the momentum equation. The ratio of specific heats γ is chosen as $5/3$ for a monoatomic gas. Weyl's gauge [26] is used while writing the induction equation for $\boldsymbol{A}$. The absence of the permeability of the free space μ_0 from the MHD equations is due to the choice of the normalization [1]. The cylindrical (or toroidal) coordinate system is used to write the physical equations where any vector is written in the orthogonal cylindrical basis as: $\boldsymbol{v} = v_R \boldsymbol{e}_R + v_Z \boldsymbol{e}_Z + v_\phi \boldsymbol{e}_\phi$.

Initial and boundary conditions

The plasma equilibrium is given by the steady and stationary ideal MHD equations. For an axisymmetric MHD equilibrium the magnetic field is defined as $\boldsymbol{B} = \nabla \times \boldsymbol{A} + F(\psi) \nabla \phi$ such that Gauss's law is satisfied exactly. Here, $F(\psi)$ is an axisymmetric equilibrium function of ψ and does not evolve in time. The Grad-Shafranov equation governs the equilibrium for stationary, axisymmetric, ideal MHD equations in terms of ψ and is written as:

$$R^2 \nabla \cdot \left(\frac{1}{R^2} \nabla \psi \right) = -F \frac{dF}{d\psi} - \frac{dp}{d\psi}$$

This is a nonlinear elliptic PDE and its solution requires the boundary data and the profiles $F(\psi)$ and $p(\psi)$. Usually this data comes from experiments. For the numerical test cases presented below the required data is taken from [18].

For the numerical tests considered here for the simple geometries, we impose Dirichlet boundary conditions on the variables at the boundaries.

4.2.1 Linear simulations

In the linear simulations presented below the magnetic energies E_n in the Fourier modes $n > 0$ are expected to grow in time exponentially at a constant rate. At each time step, these energies are computed as $\frac{1}{2} \int \frac{1}{\mu_0} \boldsymbol{B}_n \cdot \boldsymbol{B}_n \, d\Omega$ where $\boldsymbol{B}_n$ denotes the amplitude of n^{th} harmonic of the magnetic field and μ_0 denotes the vacuum permeability. The growth rates in E_n are computed using the second order finite difference formula applied in time.

Tearing modes

Tearing modes are resistive, current-driven modes that grow around a rational surface. In [18] the full MHD model was used to simulate the tearing modes and it was shown that the growth rates converge with the expected order of the accuracy as the entire grid is refined. Instead

of refining the entire grid, here we investigate the effect of the different polar treatments by clustering the polar grids near the grid center.

This test considers a circular plasma with a major radius of 10 m and a plasma radius of 1 m. As the first step in each simulation, GSE is computed on each polar grid to obtain the initial conditions. The required profiles for the equilibrium flux function are chosen as:

$$F(\psi)^2 = F_0^2 + 4(\psi_e - \psi_0)(\bar{\psi} - 0.35\bar{\psi}^2) \qquad \text{with} \qquad \bar{\psi} = \frac{\psi - \psi_0}{\psi_e - \psi_0}$$

where $F_0 = 19.45$, ψ_0 and ψ_e are the flux values at the magnetic axis and the plasma edge respectively while $\bar{\psi}$ is the normalized flux such that $\bar{\psi}$ is scaled to zero at the magnetic axis (which is also the polar grid center) and unity at the plasma boundaries. The pressure profile is specified by using the density and temperature profiles as:

$$\frac{\rho}{\rho_0} = 1 - 0.9\bar{\psi}, \qquad \frac{T}{T_0} = 1 - 0.8\bar{\psi}$$

where ρ_0 and T_0 are the values of plasma density and temperature at the magnetic axis. We choose $\rho_0 = 3.34 \times 10^{-7}$ kg.m^{-3} and $T_0 = 2.49 \times 10^5$ K. It is observed that irrespective of the polar treatment used the iterative solver to solve the GSE converge with the same number of iterations. The numerical solutions obtained with the different polar treatments have insignificant differences and this observation is consistent with the numerical tests on the elliptic (Poisson's) equation.

In the next step of each simulation, the polar grids are aligned to the magnetic flux surfaces and the resulting grids are isomorphic to the polar grids with $N_r = 101$ and $N_\theta = 70$. Starting from the numerical solution of the GSE, we evolve full MHD equations by adding small perturbations in $n = 1$ mode and by keeping $n = 0$ mode constant in time. Gear's method is used for the time integration with the time step of $\Delta t \approx 1.2967 \times 10^{-4}$ s. Tearing mode instabilities grow around a rational surface $q = 2$ which is located around the radius ≈ 0.5 m. The resistivity is set to $\eta = 1.9382 \times 10^{-6}$ Ω.m while the viscosity, particle, and heat diffusivities are set to zero.

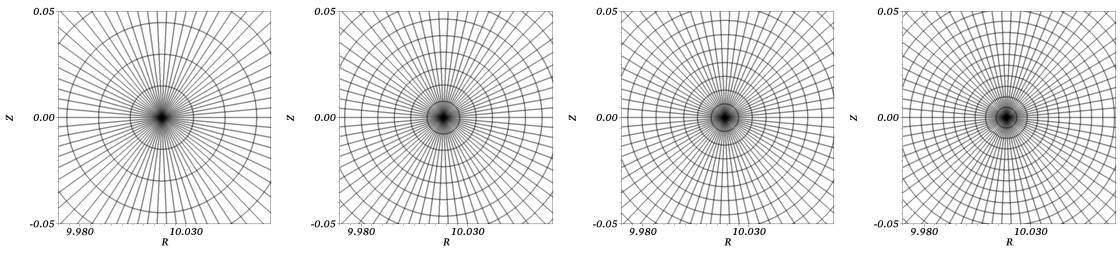

(a) Grid 0 (b) Grid 1 (c) Grid 2 (d) Grid 3

Figure 10: The series of grids used for tearing mode simulations with $N_r = 101$ and $N_\theta = 70$ with different distribution of the grid points near the polar grid center. Grid 0, 1, 2 and 3 are obtained by the clustering of the grid points at the grid center by using the clustering parameter $\sigma_1 = 999, 0.2, 0.1$ and 0.08 respectively .

The full MHD simulations are performed on the series of polar grids in which N_r and N_θ are kept the same but the clustering of the grid points is altered near the polar grid center as shown in Figure (10). JOREK allows the construction of non-equidistant grids with the possibility of clustering grid points at user-defined positions. In the parametric space, a normalized unit

domain (s) is discretized such that the distribution of the grid points is given by:

$$\mathcal{D}(\mathrm{s}) = \frac{\int_0^{\mathrm{s}} g(\zeta)\, d\zeta}{\int_0^1 g(\zeta)\, d\zeta} \tag{25}$$

where $g(\zeta)$ is a Gaussian function specified as:

$$g(\zeta) = 0.6 + 1.59576\left[\frac{1}{\sigma_1}\exp\left(\frac{-0.5(\zeta-\zeta_1)^2}{\sigma_1^2}\right) + \frac{1}{\sigma_2}\exp\left(\frac{-0.5(\zeta-\zeta_2)^2}{\sigma_2^2}\right)\right] \tag{26}$$

User-defined parameters ζ_1 and ζ_2 are used to specify two different locations around which the grid points are to be clustered whereas σ_1 and σ_2 are used to control the clustering at those locations. The location of polar grid center is identified by $\zeta_1 = 0$ while the choice of parameter $\sigma_1 = 999$, 0.2, 0.1 and 0.08 gives Grid 0, 1, 2 and 3 respectively (shown in Figure (10)). An arbitrary high number $\sigma_1 = \sigma_2 = 999$ is entered not to cluster the grid points whereas reducing σ_1 or σ_2 increases the grid point density at the respective locations ζ_1 and ζ_2.

The growth rates of the magnetic energies obtained with each grid and different polar treatments are shown in Table (1). Without any polar treatment and with C^0 treatment, the numerical solution contains the numerical noise at the grid center and steady growth rates are not obtained. In Figure (11a) the snapshot of the numerical solution obtained using C^0 treatment is shown where the tearing mode instability structures are seen along with the small region near the grid center with the numerical noise. It contributes to the computation of the growth rates and leads to wrong values. For Grid 0, the intermediate and C^1 polar treatment also show numerical noise at the grid center and the growth rates estimated are wrong. As the grid is refined near the polar grid center, clean numerical solutions are obtained and the converged values of the growth rates are obtained (see Table (1)). In Figure (11b), the numerical solutions obtained with Grid 3 are shown and it can be seen that the solution obtained is clean.

Refinement	$\mathbb{I}$	$\mathbb{T}_{C0}$	$\mathbb{T}_{C*}$	$\mathbb{T}_{C1}$
Grid 0	–	–	222.54292969955	378.150973378987
Grid 1	–	960.817436300821	215.82983095811	215.826140415818
Grid 2	–	829.437061663274	215.82867928311	215.835691745327
Grid 3	–	–	215.83175751125	215.832876025665

Table 1: Growth rates of the magnetic energies (E_1) of the tearing modes obtained on a series of polar grids with $N_r = 101$ and $N_\theta = 70$ shown in Figure (10) and different polar treatments.

To further illustrate the effect of the polar treatments, we show in Figure (12) the comparison between the evolution of the magnetic energies obtained with C^0 and C^1 polar treatments. At initial times, there is no significant difference in the two curves as the numerical solution is dominated by physical instability. Figure (13a) shows the lineout plots of A_R taken at the horizontal diameter at $t \approx 6.48$ ms and the development of the tearing mode instability structures are seen at $R \approx 9.5$ and 10.5. The numerical noise seen at the grid axis $R \approx 10$ m is orders of magnitude lower than instability structures. Later in time, the numerical noise at the grid center with C^0 polar treatment grows faster than the tearing mode instability and dominates the physical instability. This leads to the wrong estimates of the growth rates of the magnetic energies which is seen in Figure (12) after $t \approx 25$ ms. This is also evident from Figure (13b)-(13c)

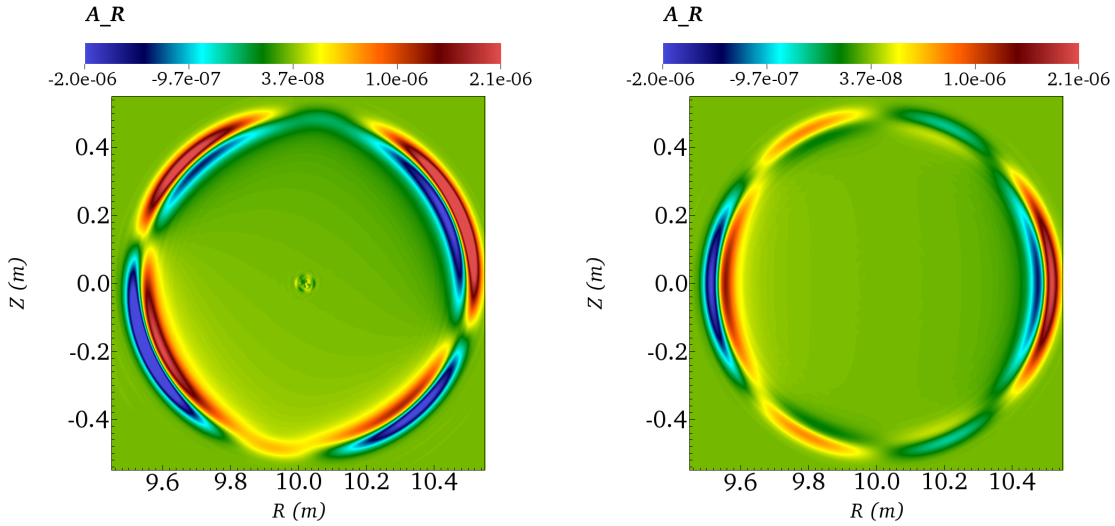

(a) (b)

Figure 11: Zoomed view of R-component of the magnetic vector potential A_R ($n = 1$) at $t \approx 32.42$ ms obtained on Grid 3 from Figure (10) with a) C^0 and b) C^1 polar treatment at the polar grid center. The former treatment yields unphysical noise at the grid center which contributes the to the wrong estimations of the growth rates.

where the lineout plots of A_R are shown at $t \approx 25.92$ and 32.48 ms and the noise at the grid center with C^0 polar treatment is seen to dominate the tearing mode instability structures. With C^1 polar treatment however the numerical noise seen at the grid center is negligibly small as compared to physical instability and remains bounded. The intermediate polar treatment gives almost identical results to the C^1 treatment and hence are not shown here in figures.

It should be noted that the physical instability structures are far from the grid center, roughly at the radius 0.5 m and the structures at the polar grid center are only a numerical artifact. The above numerical test demonstrates the strong effect of the polar treatments and grid point clustering near the grid center. The comparison of the numerical results for the different polar treatments suggests that the proposed C^1 polar treatment improves the numerical properties at the polar grid center and gives the clean numerical solution by removing the numerical noise near the grid center.

Circular ballooning modes

Ballooning modes are pressure-driven modes and instabilities associated with them occur in the region of high-pressure gradients, typically at the edge of the tokamak plasma. This test uses circular plasma with the radius of the device being 3 m and the radius of a plasma 2 m.

We evolve the single harmonic $n = 6$ by keeping the $n = 0$ mode constant in time for resistivity specified to $\eta = 1.9382 \times 10^{-6}$ Ω.m while the viscosity is set to zero. The particle diffusion perpendicular to the magnetic field is set to 1.54 $m^2.s^{-1}$. The parallel and perpendicular heat diffusivities are set to 0.516 and 5.16×10^{-7} $kg.m^{-1}.s^{-1}$ respectively.

A series of polar grids is constructed with $N_r = 51$ and $N_\theta = 65$ at the different levels of refinement at the polar grid center by specifying the clustering parameter $\sigma_1 = 999, 0.2, 0.15$ and 0.1 and are shown in Figure (14). Once again the test is designed to highlight the effect

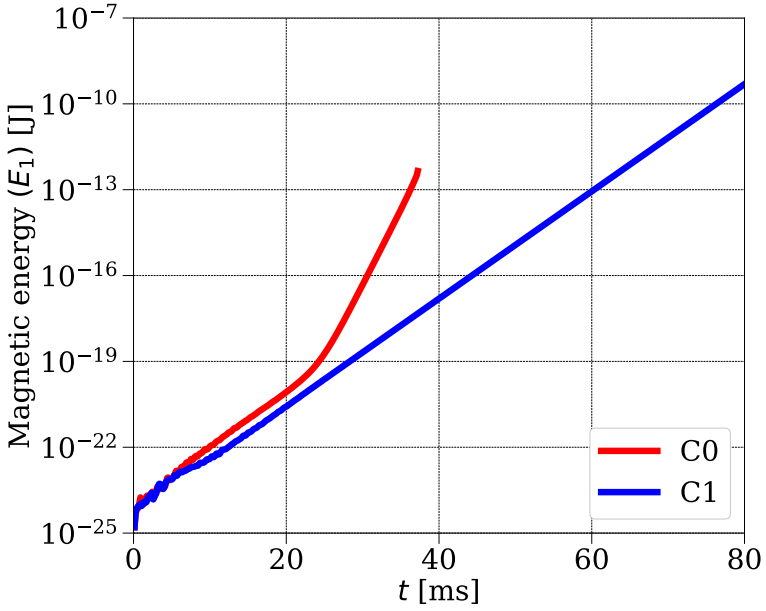

Figure 12: Evolution of the magnetic energy in $n = 1$ harmonic in the tearing mode simulation performed on Grid 3. At initial times both treatments follow the growth of physical instabilities. Later, the numerical instabilities are seen at the grid center with C^0 polar treatment that dominates the physical instabilities.

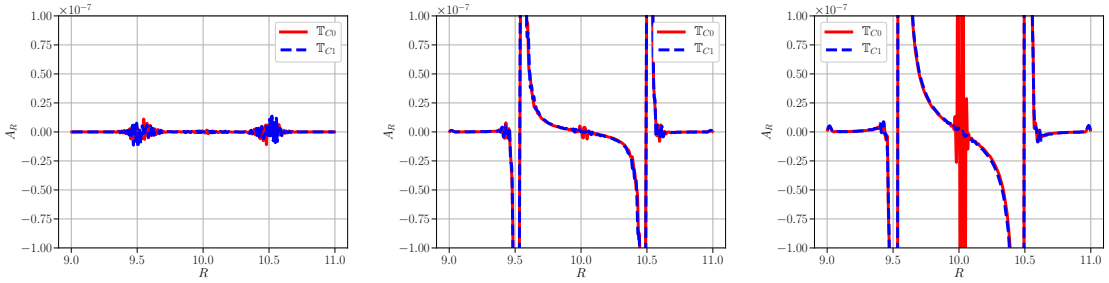

(a) $t \approx 6.48$ ms (b) $t \approx 25.92$ ms (c) $t \approx 32.42$ ms

Figure 13: Comparison of the lineout plots for the perturbations in A_R along the horizontal diameter of the polar grid obtained using C^0 and C^1 polar treatments.

of the refinement at the grid center and the polar treatments. The computations are performed for all the polar treatments under discussion and show no significant difference in the numerical solution of the GSE which serves as the initial condition for the full MHD computations. Gear's method is used for the time integration with the time step of $\Delta t = 6.4836 \times 10^{-6}$ s to compute the evolution of the circular ballooning modes. The results with no special polar treatment and C^0 treatment are dominated by the numerical noise at the grid center with all four grids and are not shown here. Below we show the comparison between the intermediate and C^1 treatments.

Figure (15a) shows the initial temperature profile used for the circular ballooning mode simulations along with a polar grid while a constant density profile is used. The ballooning

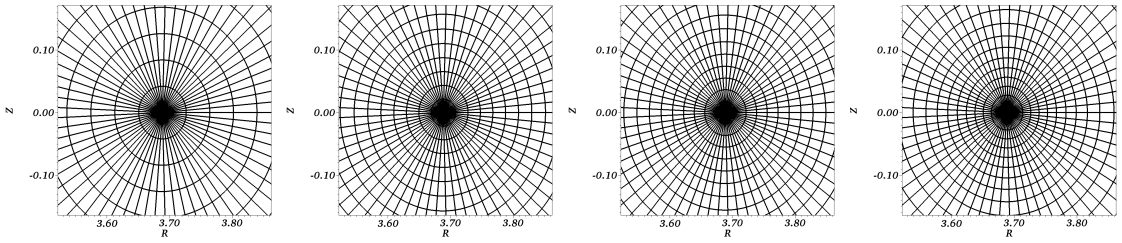

(a) Grid 0 (b) Grid 1 (c) Grid 2 (d) Grid 3

Figure 14: The series of grids used for the circular ballooning mode simulations with $N_r = 51$ and $N_\theta = 65$ with different distribution of the grid points near the polar grid center. Grid 0, 1, 2 and 3 are obtained by the clustering of the grid points at the grid center by using the clustering parameter $\sigma_1 = 999, 0.2, 0.15$ and 0.1 respectively .

mode instabilities are expected to occur around the gradient in the pressure. The grids are aligned to the magnetic flux iso-surfaces and the grid center is located at the magnetic axis at $R \approx 3.68$ and $Z = 0$. Figure (15b) shows the comparison of the growth rates obtained on the series of grids (see Figure (14)) using the intermediate and C^1 polar treatments. It is seen that C^1 treatment converges faster than the intermediate polar treatment as the grid is refined at the polar center. Using Grid 3 both treatments give nearly identical growth rates and clean numerical solutions at the polar center. The data point for growth rate on Grid 2 with intermediate polar treatment is taken from an initial small time interval over which the growth rate is constant. At later times numerical noise at the polar center pollutes the numerical solution and growth rates deviate from the shown value (similar to that with Figure (12) in the case of tearing modes simulation). Using Grid 0 and 1 the intermediate treatment gives the solution dominated by the numerical noise at the grid center.

In Figure (16) the perturbations in the magnetic flux $\psi = RA_\phi$ computed on Grid 0 with the intermediate and C^1 polar treatments are plotted in the same scale and at $t \approx 1.29$ ms. In both figures, the ballooning mode structures are seen at the location of the pressure gradient. In Figure (16a) however, the numerical noise is seen surrounding the grid center whose maximum value is of the order 10^{-3}. The numerical noise is seen to spread in the region surrounding the grid center and has dominated the numerical solution. This leads to the wrong estimates of the growth rates. Figure (16b) shows that C^1 polar treatment gives clean numerical solution with Grid 0. As the grid is refined at the polar center, the noise obtained with the intermediate treatment at the grid center reduces and it gives nearly identical results to that with C^1 treatment.

The intermediate treatment gives clean solutions if the grid is sufficiently resolved near the grid center while C^1 gives cleaner solutions on the relatively coarse grids near the grid center. This numerical test highlights the improvement of the stability and accuracy of the numerical method at the polar grid center due to the use of the proposed treatment.

4.2.2 Nonlinear simulations

In subsections above, we presented linear MHD simulations where locations of the physical instabilities are far from the polar grid center. In this subsection, we present a nonlinear simulation for internal kink modes where plasma undergoes a nonlinear saturation phase. The diffusivities are chosen such that the cyclic dynamics of kink modes is seen in the nonlinear saturation phase and dynamics occur across the grid center. The simulation is performed with C^1 polar treatment applied at the grid center.

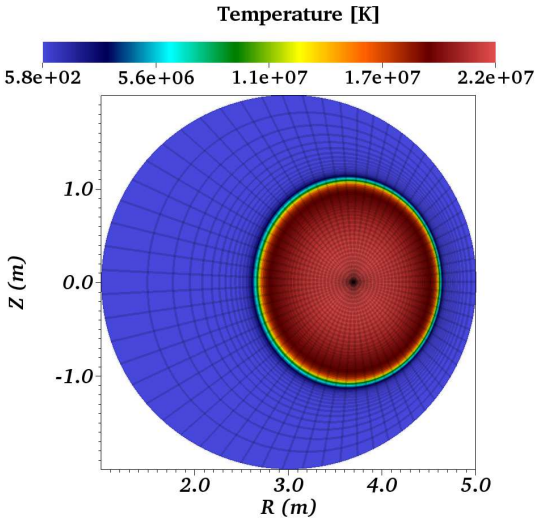

(a)

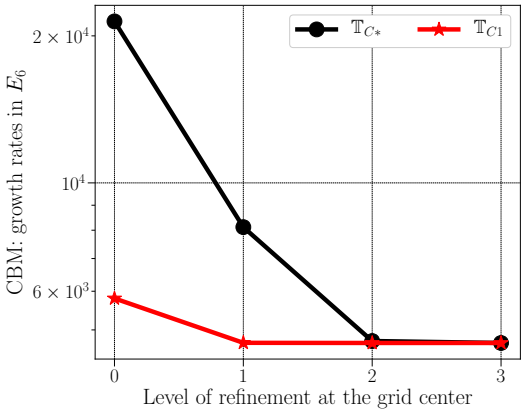

(b)

Figure 15: a) The initial temperature profile for circular ballooning modes plotted with the polar grid. b) Growth rates plotted for circular ballooning modes $n = 6$ for the intermediate and C^1 polar treatment for the different levels of the refinement at the polar grid center as shown in Figure (14).

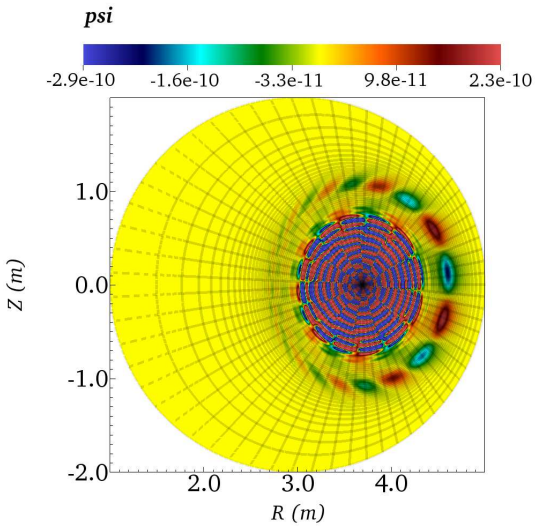

(a)

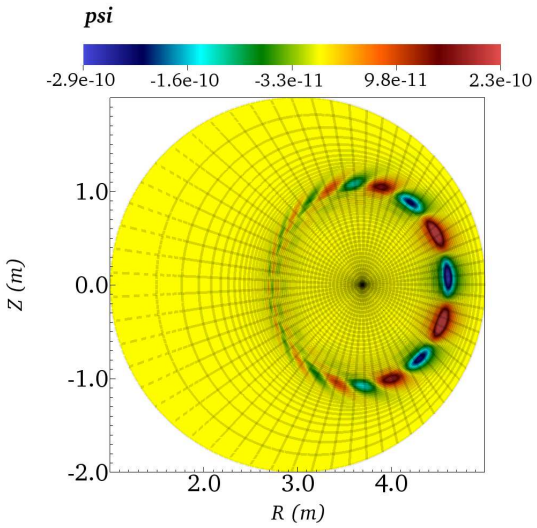

(b)

Figure 16: Circular ballooning mode instability structures in the magnetic flux $\psi = R\ A_\phi$ for $n = 6$ with the a) intermediate and b) C^1 polar treatment obtained on the Grid 0 from Figure (14).

Internal kink modes are resistive, current-driven modes that grow around a rational surface $q = 1$. We consider a circular plasma with a major radius of 10 m and a plasma radius of 1 m.

The required profiles for the GSE to compute the equilibrium are chosen as:

$$F(\psi)^2 = F_0^2 + 4(\psi_e - \psi_0)(\bar{\psi} - 0.35\bar{\psi}^2) \qquad \text{with} \qquad \bar{\psi} = \frac{\psi - \psi_0}{\psi_e - \psi_0}$$

where $F_0 = 12$. The pressure profile is specified by using the density and temperature profiles as:

$$\frac{\rho}{\rho_0} = 1 - 0.9\bar{\psi}, \qquad \frac{T}{T_0} = 1 - 0.8\bar{\psi}$$

We choose $\rho_0 = 3.34\times10^{-7}$ kg.m^{-3} and $T_0 = 1.15\times10^{6}$ K. The polar grid aligned to the magnetic flux surfaces is used with $N_r = 60$ and $N_\theta = 60$ and C^1 treatment is applied at the grid center. Starting from the numerical solution of the GSE, we evolve full MHD equations by adding small perturbations in $n = 1, 2, 3$ modes and using Gear's method for the time integration. For this configuration, the rational surface $q = 1$ is located at the radial location $\zeta_2 = 0.42$ where the grid is locally refined by specifying the refinement parameter $\sigma_2 = 0.1$ to resolve the kink instability structures. The grid is refined at the polar grid center $\zeta_1 = 0$ as well by specifying $\sigma_1 = 0.1$.

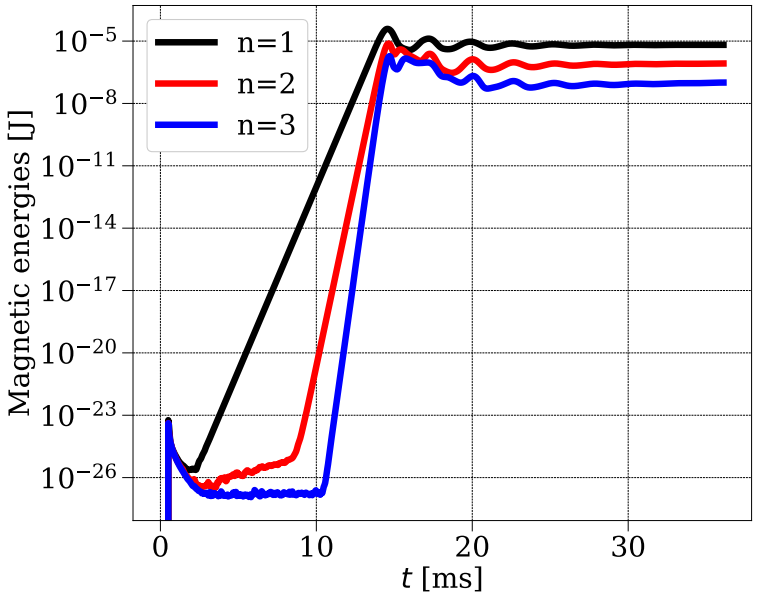

Figure 17: Evolution of the magnetic energies for $n > 0$ in the nonlinear kink mode simulation. After exponential growth, the modes undergo cyclic kink dynamics in nonlinear saturation phase.

The constant value of resistivity is set to $\eta = 1.9382 \times 10^{-5}$ Ω.m while the viscosity is set to $\mu = 5.16 \times 10^{-6}$ kg.m^{-1}.s^{-1}. The particle diffusion perpendicular to the magnetic field is set to 0.15 m^2.s^{-1}. The perpendicular heat diffusivity is set to 5.16×10^{-7} kg.m^{-1}.s^{-1} while parallel heat diffusivity is set to zero. Figure (17) shows the evolution of magnetic energies in $n > 0$ modes for the nonlinear simulation plotted in semi-log scale. Until $t \approx 15$ ms we can see the exponential growth in the magnetic energies in $n > 0$ modes. In this phase, as expected, $n > 0$ modes grow exponentially such that the dynamics is always dominated by lower modes. Figure (18) shows snapshots of the magnetic flux ψ at some time instants. At beginning of the

saturation phase, the profile of ψ begins to deform as seen in Figure (18b). Beyond this point nonlinearities become dominant and the plasma exhibits cyclic kink dynamics as seen in Figure (17) beyond $t \approx 15$ ms. Figure (18c) shows ψ field plotted in the saturation phase at $t \approx 22.25$ ms showing the variations in the numerical solution at the polar grid center. The C^1 polar treatment applied here does not show any sign of instability or numerical noise at the polar grid center and the simulation continues for a long time.

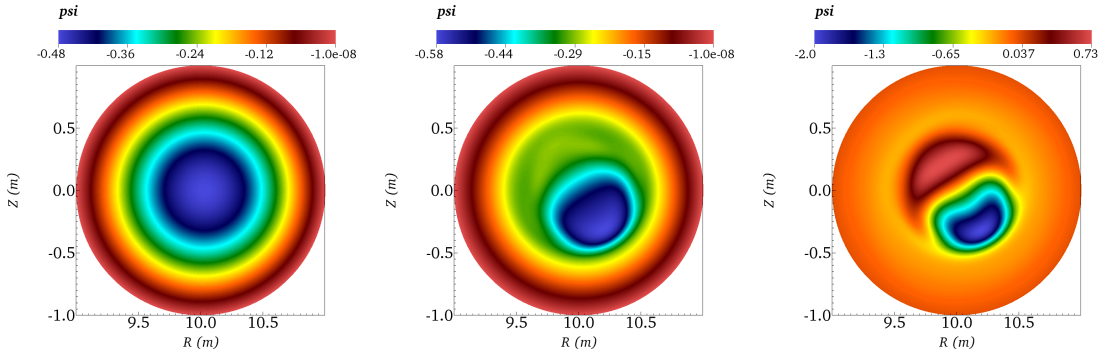

(a) $t = 0$ ms (b) $t = 14.61$ ms (c) $t = 22.25$ ms

Figure 18: Snapshots of ψ field shown at the mentioned time instants from nonlinear internal kink simulation performed using C^1 polar treatment. The numerical solution exhibits a motion across the polar grid center and no sign of the numerical instability is seen at the polar grid center.

5 Summary and Conclusions

Grid generation is an important step in computational applications. Grids decide the numerical properties, such as the stability and accuracy, of the numerical methods for a problem to be solved. It is well known that grids should be constructed in a manner such that there are no sudden variations in the numerical properties of the discretization methods. In this work, we have investigated the applications of the bi-cubic Hermite Bézier FEM on the polar grids. At the polar grid center, the bi-cubic Hermite Bézier FEM is not well defined. The numerical properties of the FEM degrade and lead to the sudden variation at the polar grid center as compared to the surrounding vertices. Evidently, the bi-cubic Hermite Bézier FEM leads to spurious oscillations at the polar grid center, especially in absence of any stabilization mechanism. Some of the crude polar treatments have been used so far to enforce C^0 regularity at the grid center however, the polar grid center remains susceptible to numerical difficulties.

In this work, we have developed a mathematically consistent numerical treatment to enforce C^1 regularity at the polar grid center for the bi-cubic Hermite-Bézier FEM in the isoparametric framework. The proposed treatment involves the application of the new basis functions at the grid center which are simply the linear transformation of the original basis functions and its implementation is straightforward. The treatment also preserves the accuracy of the interpolation at the polar grid center. With the help of a range of numerical tests, it is demonstrated that the proposed treatment improves the numerical properties of the bi-cubic Hermite Bézier FEM at the polar grid center. In presence of numerical or physical stabilization mechanisms, however, the polar grid center is found to be 'well behaved' even with the crude ways of polar treatments. The role of the proposed polar treatment to correctly and optimally simulate the MHD instabilities is highlighted. The proposed treatment is valid for any isomorphic polar grid with the isoparametric bi-cubic Hermite Bézier FEM as well as the classical cubic Hemite FEM, where latter is a special case of the former. The treatment has been implemented in the computational setup of the code JOREK and can be helpful in the simulations of MHD flows on the polar grids.

The bi-cubic Hermite Bézier FEM guarantees C^1 regularity across the elements when one vertex is shared by four elements. In certain situations, a vertex may be shared by more than four elements where many blocks of a grid are patched together. This is particularly the case in the grid aligned to the magnetic flux iso-surfaces when the plasma equilibrium has a saddle point, also known as X-point, at which a vertex is shared by eight elements. At such locations, bi-cubic Hermite Bézier FEM is not well defined. The approach used in this work for the singular polar grid center can be extended to other such singular points where the gradients and second derivatives in the physical space can be used as a new set of variables. The approach can also be extended to the recently implemented higher-order extensions of the Hermite Bézier FEM [21].

Acknowledgment

This work has been carried out within the framework of the EUROfusion Consortium, funded by the European Union via the Euratom Research and Training Programme (Grant Agreement No 101052200 — EUROfusion). Views and opinions expressed are however those of the author(s) only and do not necessarily reflect those of the European Union or the European Commission. Neither the European Union nor the European Commission can be held responsible for them.

References

[1] M. Hoelzl, G. Huijsmans, S. Pamela, M. Bécoulet, E. Nardon, F. Artola, B. Nkonga, C. Atanasiu, V. Bandaru, A. Bhole, D. Bonfiglio, A. Cathey, O. Czarny, A. Dvornova, T. Fehér, A. Fil, E. Franck, S. Futatani, M. Gruca, H. Guillard, J. Haverkort, I. Holod, D. Hu, S. Kim, S. Korving, L. Kos, I. Krebs, L. Kripner, G. Latu, F. Liu, P. Merkel, D. Meshcheriakov, V. Mitterauer, S. Mochalskyy, J. Morales, R. Nies, N. Nikulsin, F. Orain, J. Pratt, R. Ramasamy, P. Ramet, C. Reux, K. Särkimäki, N. Schwarz, P. S. Verma, S. Smith, C. Sommariva, E. Strumberger, D. van Vugt, M. Verbeek, E. Westerhof, F. Wieschollek, and J. Zielinski, "The JOREK non-linear extended MHD code and applications to large-scale instabilities and their control in magnetically confined fusion plasmas," Nuclear Fusion, vol. 61, p. 065001, may 2021.

[2] M. D. Griffin, E. Jones, and J. D. Anderson, "A computational fluid dynamic technique valid at the centerline for non-axisymmetric problems in cylindrical coordinates," Journal of Computational Physics, vol. 30, no. 3, pp. 352–360, 1979.

[3] K. Mohseni and T. Colonius, "Numerical Treatment of Polar Coordinate Singularities," Journal of Computational Physics, vol. 157, no. 2, pp. 787–795, 2000.

[4] G. Constantinescu and S. Lele, "A Highly Accurate Technique for the Treatment of Flow Equations at the Polar Axis in Cylindrical Coordinates Using Series Expansions," Journal of Computational Physics, vol. 183, no. 1, pp. 165–186, 2002.

[5] B. Prochnow, O. O'Reilly, E. M. Dunham, and N. A. Petersson, "Treatment of the polar coordinate singularity in axisymmetric wave propagation using high-order summation-by-parts operators on a staggered grid," Computers & Fluids, vol. 149, pp. 138–149, 2017.

[6] R. D. Sandberg, "An axis treatment for flow equations in cylindrical coordinates based on parity conditions," Computers & Fluids, vol. 49, no. 1, pp. 166–172, 2011.

[7] W. Huang and D. M. Sloan, "Pole Condition for Singular Problems: The Pseudospectral Approximation," Journal of Computational Physics, vol. 107, no. 2, pp. 254–261, 1993.

[8] E. Serre and J. Pulicani, "A three-dimensional pseudospectral method for rotating flows in a cylinder," Computers & Fluids, vol. 30, no. 4, pp. 491–519, 2001.

[9] I. Mercader, O. Batiste, and A. Alonso, "An efficient spectral code for incompressible flows in cylindrical geometries," Computers & Fluids, vol. 39, no. 2, pp. 215–224, 2010.

[10] R. Asaithambi and K. Mahesh, "A Note on a Conservative Finite Volume Approach to Address Numerical Stiffness in Polar Meshes," J. Comput. Phys., vol. 341, p. 377–385, jul 2017.

[11] L. G. Olson, G. C. Georgiou, and W. W. Schultz, "An efficient finite element method for treating singularities in Laplace's equation," Journal of Computational Physics, vol. 96, no. 2, pp. 391–410, 1991.

[12] R. Oguic, S. Viazzo, and S. Poncet, "A parallelized multidomain compact solver for incompressible turbulent flows in cylindrical geometries," Journal of Computational Physics, vol. 300, pp. 710–731, 2015.

[13] D. Toshniwal, H. Speleers, R. R. Hiemstra, and T. J. Hughes, "Multi-degree smooth polar splines: A framework for geometric modeling and isogeometric analysis," Computer Methods in Applied Mechanics and Engineering, vol. 316, pp. 1005–1061, 2017. Special Issue on Isogeometric Analysis: Progress and Challenges.

[14] D. Toshniwal and T. J. Hughes, "Isogeometric discrete differential forms: Non-uniform degrees, Bézier extraction, polar splines and flows on surfaces," Computer Methods in Applied Mechanics and Engineering, vol. 376, p. 113576, 2021.

[15] F. Holderied and S. Possanner, "Magneto-hydrodynamic eigenvalue solver for axisymmetric equilibria based on smooth polar splines," Journal of Computational Physics, vol. 464, p. 111329, 2022.

[16] O. Czarny and G. Huysmans, "Bézier surfaces and finite elements for MHD simulations," Journal of Computational Physics, vol. 227, no. 16, pp. 7423–7445, 2008.

[17] H. Grad and H. Rubin, "Hydromagnetic equilibria and force-free fields," 10 1958.

[18] S. J. P. Pamela, A. Bhole, G. T. A. Huijsmans, B. Nkonga, M. Hoelzl, I. Krebs, and E. Strumberger, "Extended full-MHD simulation of non-linear instabilities in tokamak plasmas," Physics of Plasmas, vol. 27, no. 10, p. 102510, 2020.

[19] M. Wu, B. Mourrain, A. Galligo, and B. Nkonga, "H1-parametrizations of complex planar physical domains in isogeometric analysis," Computer Methods in Applied Mechanics and Engineering, vol. 318, pp. 296–318, 2017.

[20] M. Wu, Y. Wang, B. Mourrain, B. Nkonga, and C. Cheng, "Convergence rates for solving elliptic boundary value problems with singular parameterizations in isogeometric analysis," Computer Aided Geometric Design, vol. 52-53, pp. 170–189, 2017. Geometric Modeling and Processing 2017.

[21] S. Pamela, G. Huijsmans, and M. Hoelzl, "A generalised formulation of G-continuous Bézier elements applied to non-linear MHD simulations," Journal of Computational Physics, vol. 464, p. 111101, 2022.

[22] S. Pamela, G. Huijsmans, A. Thornton, A. Kirk, S. Smith, M. Hoelzl, and T. Eich, "A wall-aligned grid generator for non-linear simulations of MHD instabilities in tokamak plasmas," Computer Physics Communications, vol. 243, pp. 41–50, 2019.

[23] H. Guillard, J. Lakhlili, A. Loseille, A. Loyer, B. Nkonga, A. Ratnani, and A. Elarif, "Tokamesh : A software for mesh generation in Tokamaks," Research Report RR-9230, CASTOR, Dec. 2018.

[24] G. Giorgiani, H. Bufferand, F. Schwander, E. Serre, and P. Tamain, "A high-order non field-aligned approach for the discretization of strongly anisotropic diffusion operators in magnetic fusion," Computer Physics Communications, vol. 254, p. 107375, 2020.

[25] G. Giorgiani, H. Bufferand, G. Ciraolo, P. Ghendrih, F. Schwander, E. Serre, and P. Tamain, "A hybrid discontinuous Galerkin method for tokamak edge plasma simulations in global realistic geometry," Journal of Computational Physics, vol. 374, pp. 515–532, 2018.

[26] J. Haverkort, H. Blank, G. Huijsmans, J. Pratt, and B. Koren, "Implementation of the full viscoresistive magnetohydrodynamic equations in a nonlinear finite element code," Journal of Computational Physics, pp. 281–302, 04 2016.

[27] E. Anderson, Z. Bai, C. Bischof, S. Blackford, J. Demmel, J. Dongarra, J. Du Croz, A. Greenbaum, S. Hammarling, A. McKenney, and D. Sorensen, LAPACK Users' Guide. Philadelphia, PA: Society for Industrial and Applied Mathematics, third ed., 1999.

[28] R. Codina, "A discontinuity-capturing crosswind-dissipation for the finite element solution of the convection-diffusion equation," Computer Methods in Applied Mechanics and Engineering, vol. 110, no. 3, pp. 325–342, 1993.

[29] R. M. Beam and R. F. Warming, "Alternating Direction Implicit Methods for Parabolic Equations with a Mixed Derivative," SIAM Journal on Scientific and Statistical Computing, vol. 1, no. 1, pp. 131–159, 1980.

[30] J. P. Freidberg, Ideal MHD. Cambridge University Press, 2014.